MNRAS 000, 1–18 (2022) Preprint 21 August 2023 Compiled using MNRAS LATEX style file v3.0

THESAN-HR: How does reionization impact early galaxy evolution?

Josh Borrow,[1]★ Rahul Kannan,[2] Enrico Garaldi,[3] Aaron Smith,[2,1] Mark Vogelsberger,[1,4] Rüdiger Pakmor,[3] Volker Springel,[3] and Lars Hernquist[2]

[1]Department of Physics and Kavli Institute for Astrophysics and Space Research, Massachusetts Institute of Technology, Cambridge, MA 02139, USA
[2]Center for Astrophysics | Harvard & Smithsonian, 60 Garden Street, Cambridge, MA 02138, USA
[3]Max-Planck Institute for Astrophysics, Karl-Schwarzschild-Str. 1, D-85741 Garching, Germany
[4]The NSF AI Institute for Artificial Intelligence and Fundamental Interactions, Massachusetts Institute of Technology, Cambridge MA 02139, USA

Accepted XXX. Received YYY; in original form ZZZ

arXiv:2212.03255v2 [astro-ph.GA] 17 Aug 2023

ABSTRACT

The feedback loop between the galaxies producing the background radiation field for reionization and their growth is crucial, particularly for low-mass haloes. Despite this, the vast majority of galaxy formation studies employ a spatially-uniform, time-varying reionizing background, with the majority of reionization studies employing galaxy formation models only required to work at high redshift. This paper uses the well-studied TNG galaxy formation model, calibrated at low redshift, coupled to the Arepo-RT code, to self-consistently solve the coupled problems of galaxy evolution and reionization, evaluating the impact of patchy (and slow) reionization on early galaxies. THESAN-HR is an extension of the THESAN project to higher resolution (a factor of 50 increase, with a baryonic mass of $m_{\rm b} \approx 10^4$ M$_\odot$), to additionally enable the study of 'mini-haloes' with virial temperatures $T_{\rm vir} < 10^4$ K. Comparing the self-consistent model to a uniform UV background, we show that galaxies in THESAN-HR are predicted to be larger in physical extent (by a factor ~ 2), less metal enriched (by ~ 0.2 dex), and less abundant (by a factor ~ 10 at $M_{1500} = -10$) by $z = 5$. We show that differences in star formation and enrichment patterns lead to significantly different predictions for star formation in low mass haloes, low-metallicity star formation, and even the occupation fraction of haloes. We posit that cosmological galaxy formation simulations aiming to study early galaxy formation ($z \gtrsim 3$) must employ a spatially inhomogeneous UV background to accurately reproduce galaxy properties.

Key words: Galaxies: formation; Galaxies: evolution; Cosmology: dark ages, reionization, first stars; Methods: numerical

1 INTRODUCTION

Just after the Big Bang, the Universe was filled with a hot, dense, plasma, where radiation and matter were in thermal equilibrium equilibrium. As the Universe expanded and cooled, electrons and protons could recombine, filling the Universe with a primordial mixture of neutral hydrogen and helium. In this early state, small overdensities began to grow under their own self-gravity, beginning the process of cosmological structure formation. As gas accreted into dark matter haloes, cooling down to temperatures low enough to form molecular hydrogen, the first stars were born. These massive, hot, and bright Population (Pop) III stars produced copious amounts of ionizing radiation, which began the process of reionizing the Universe. As the abundance of stars in galaxies grew, the most massive galaxies were able to reionize the Universe, fully ionizing the intergalactic medium (IGM), leaving it in equilibrium with the background radiation field once again, at a temperature of $T \sim 10^4$ K (see Wise 2019; Gnedin & Madau 2022, for an extensive review of reionization).

Understanding the process of reionization is central to our understanding of the evolution of the early Universe, but at the core of the common description (as above) is a circular argument – galaxies are made out of cold, neutral, gas, but they destroy and suppress the formation of such gas. In addition, as ionization fronts proceed outwards from galaxies, and can only travel as quickly as they can ionize gas, reionization is expected to be patchy, rather than spatially uniform. It is well understood how such patchy reionization models can impact the filamentary structures between galaxies and the IGM more generally, with areas that are reionized earlier having lower densities due to additional photoheating pressure (Gnedin & Hui 1998; Theuns et al. 2000; Schaye et al. 2000; Kulkarni et al. 2015; Rorai et al. 2017; Wu et al. 2019; Katz et al. 2020; Puchwein et al. 2022). Strong radiation fields are also expected to reduce the fraction of baryons that galaxies can retain, further suppressing galaxy growth, as well as influencing the makeup of the multiphase interstellar medium (Wise & Abel 2008; Wise et al. 2012a; Wu et al. 2019; Katz et al. 2020).

Despite this, most cosmological galaxy formation simulations typically employ a time varying, but spatially-uniform, ultraviolet background (UVB) to model the photoionizing feedback from their constituent stars. These models are entirely fixed, and not self-consistent with the constituents of the simulation (Haardt & Madau 1996, 2001; Faucher-Giguère et al. 2009; Dubois et al. 2012; Vogelsberger et al. 2013; Schaye et al. 2015; Ploeckinger & Schaye 2020). Typically, this approach adopts a fixed 'reionization redshift', often $z_{\rm reion} \approx 10$, where all gas in the simulation is exposed to a strong UV

★ E-mail: josh@joshborrow.com, borrowj@mit.edu (JB)

© 2022 The Authors

background following these time-varying models, whereas at prior times the gas is considered to be shielded. This approximation is certainly valid at present times, where all gas will have been exposed to such radiation fields for many billions of years, when typical galaxy formation models are employed (the EAGLE model forms 90% of its stellar mass in the time between $z = 2$ and $z = 0$; Crain et al. 2015). During (and shortly after) the first epoch of galaxy formation, however, such approximations are not likely to be valid. As we enter the epoch of the *JWST*, and galaxy formation studies move to redshifts $z > 3$ (with galaxy surveys such as *JADES*), we must re-examine the impact of reionization on our galaxy formation models (Kannan et al. 2022a).

There have been many studies that attempt to model reionization consistently with galaxy formation simulations by post-processing the outputs, using the gas density field and stellar masses along with either an approximate method (e.g. excursion set formalism, dark matter, or gas; Santos et al. 2010; Mesinger et al. 2011; Hassan et al. 2016; Whitler et al. 2020) or a radiative transfer (RT) calculation (Baek et al. 2010; Ciardi et al. 2012; Graziani et al. 2015; Ross et al. 2017; Eide et al. 2018; Hassan et al. 2022) to estimate the speed of ionization fronts and morphologies of the ionized bubbles in the early universe. This approach is sensitive to many factors, not least the escape fractions of photons from galaxies which are still relatively unconstrained (Kostyuk et al. 2022; Yeh et al. 2022; Rosdahl et al. 2022), or the impact of dust on galaxy luminosity predictions (Vogelsberger et al. 2020; Shen et al. 2020, 2022), but can typically perform RT calculations at high accuracy (with many frequency bins), and in much larger volumes than those that use fully-coupled RT to *self-consistently* study reionization.

Fully self-consistent simulations of reionization require on-the-fly coupling of RT, hydrodynamics, and cooling calculations. Because of the requirement to effectively sample the *light*-crossing timescale (rather than the sound-crossing timescale required for hydrodynamics calculations), such models are extremely computationally intensive, an order of magnitude more computing time than hydrodynamical calculations, even when employing a reduced speed of light approximation (Kannan et al. 2022b). Despite this additional cost, such simulations are extremely fruitful, and there are a handful of models available today for use by the community. These schemes either target a self-consistent description of the largest scales with boxes $L_{\rm box} \gtrapprox 100$ Mpc at relatively low resolution (O'Shea et al. 2015; Ocvirk et al. 2016, 2020), with recent models increasing in resolution significantly to track even the formation of dwarfs (Kannan et al. 2022b; Smith et al. 2022; Garaldi et al. 2022; Rosdahl et al. 2022), or aim to target the formation of individual dwarf galaxies or small volumes (Petkova & Springel 2011; Gnedin 2014; So et al. 2014; Gnedin 2016a; Pawlik et al. 2017; Semelin et al. 2017; Trebitsch et al. 2017; Rosdahl et al. 2018; Pallottini et al. 2019; Obreja et al. 2019; Wu et al. 2019; Pallottini et al. 2022). In this paper, we aim to extend one of these large-volume suites, THESAN (Kannan et al. 2022b; Smith et al. 2022; Garaldi et al. 2022), down to even lower masses and higher resolutions (with a resolution increase of a factor 100) using the same model to span halo mass scales of $10^6 < M_{\rm H}/{\rm M}_\odot < 10^{12}$ at $z = 6$.

Simulating to low mass scales is crucial to fully understand the galaxy-reionization connection. Haloes with a virial temperature $T_{\rm vir} < 10^4$ K (circular velocities $V_c < 30$ km s^{-1}, ${\rm M_H} \approx 10^8$ M$_\odot$ at $z = 5$, also known as 'minihaloes') are susceptible to photoevaporation from the UV background, as photoheated HII gas in ionization equilibrium is typically around this temperature (Rees 1986; Shapiro et al. 2004; Iliev et al. 2005). As such, galaxy formation simulations with a resolution too low to model these haloes will miss out on a population of galaxies that are highly impacted by reionization physics. Other consequences of photoheating, such as prolonged cooling times, or preventative feedback, are less affected by the specific choice of mass scale, though clearly will be more efficient in lower-mass objects (Efstathiou 1992; Shapiro et al. 1994; Gnedin 2000; Hoeft et al. 2006; Okamoto et al. 2008; Gnedin & Kaurov 2014; Katz et al. 2020). These haloes are additionally influenced by streaming velocities between gas and dark matter, though this is expected to be a subdominant effect (Milosavljević & Bromm 2014; Schauer et al. 2022).

To fully understand the impact of our choice of reionization treatment, we perform simulations using `Arepo-RT` (Kannan et al. 2019) and the fiducial THESAN model, as used in the THESAN-1 simulation volume. We choose to compare two scenarios: the typical Faucher-Giguère et al. (2009) time-varying, but spatially-uniform UVB used in most cosmological galaxy formation simulations, and the fully self-consistent model from THESAN, to investigate what physics simulations employing a spatially uniform UVB are missing. These two scenarios also can correspond to two different fields: one near a massive, highly ionizing object (the uniform UVB), and one without, where the radiation from low mass sources dominates (our THESAN model).

The paper is organised as follows: in section 2, we describe our simulation model, choice of simulation volume, and some global properties of our volumes over time. To demonstrate in detail the impact of reionization treatments on cumulative galaxy properties, such as the UV luminosity function, we show various scaling relations in section 3. In section 4, we tie these differing galaxy properties to different gas phase evolution between the reionization treatments, and in section 5 we summarise and conclude.

2 SIMULATIONS

In this paper we explore two classes of models: simulations with a typical, spatially-uniform, but time-varying UV background, and simulations that include a self-consistent treatment using the same on-the-fly radiative transfer code as in the main THESAN project. We perform simulations with the exact same initial conditions, the same underlying physical model (including nonequlibrium chemistry), and the same output strategy, in all cases, with the only difference being our choice of reionization treatment (here referred to as our 'reionization model'). In this section we describe both the model and simulation volumes that we will use throughout the paper.

In Fig. 1 we show the large-scale gas temperature distribution at redshift $z = 7$ for these two models. The top right part of the image shows the THESAN-HR volume, which contains much colder regions with temperatures $T < 10^3$ K that are not possible in the Uniform UVB simulation due to the uniform photoheating of the gas. This leads additionally to there being much denser (and spatially thinner) cold filaments in THESAN, though the hot collisionally ionized regions that are heated by stellar feedback remain roughly consistent between the two models. This overall picture is consistent with prior work on patchy reionization, e.g. Puchwein et al. (2022).

In the circles, we show the HI gas in the most massive galaxy (halo mass $M_{\rm H} \approx 5 \times 10^{10}$ M$_\odot$, stellar mass $M_* \approx 1 \times 10^8$ M$_\odot$) in the volume. In the Uniform UVB model this gas is produced through self-shielding using the prescription from Rahmati & Schaye (2014). In THESAN, self-shielding is calculated self-consistently from the radiation fields and recombination rates of the ionized gas. This leads to differing HI gas content, with THESAN showing a factor of ~ 10

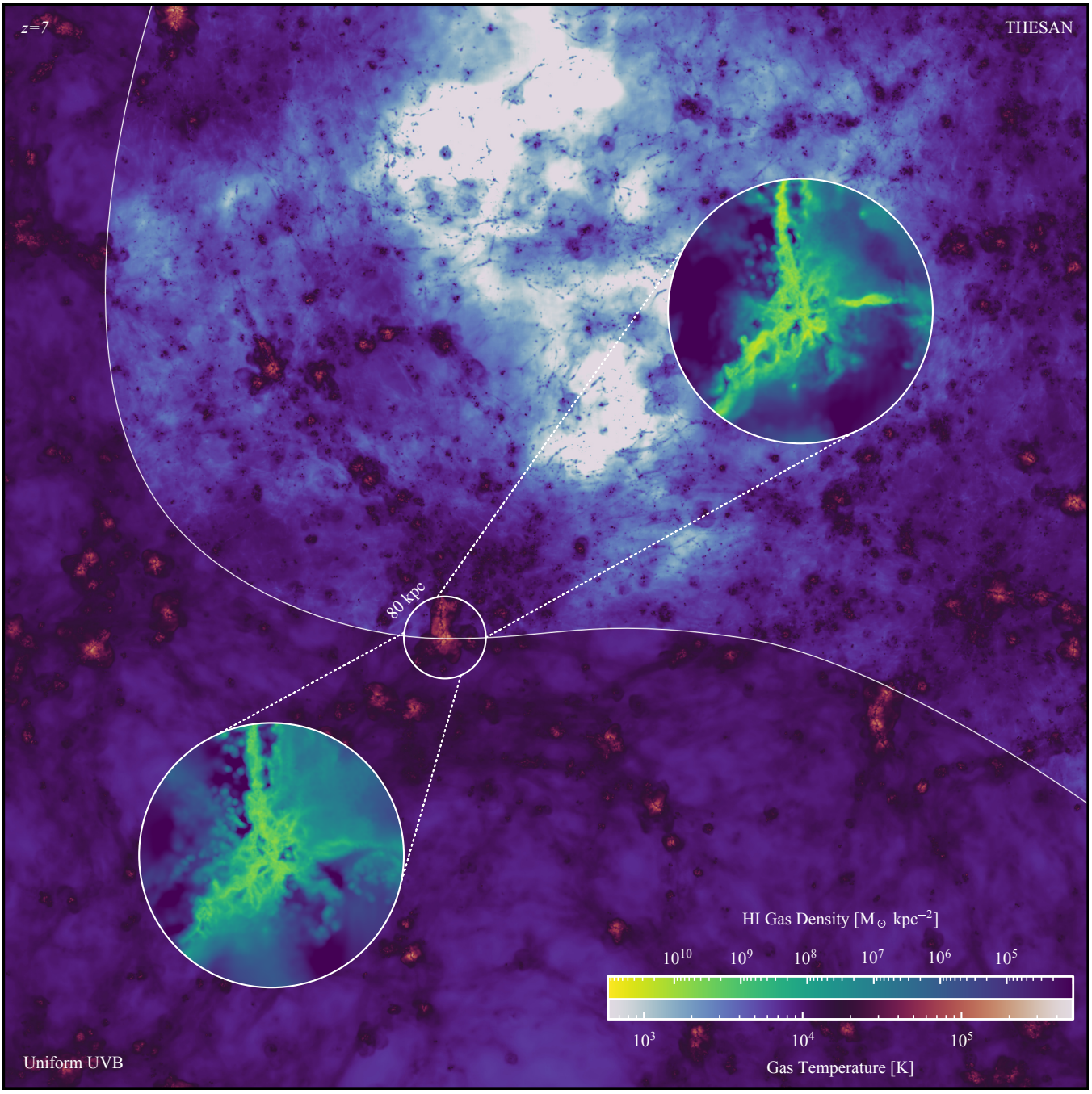


Figure 1. A projection through the entire L8N512 volume, at redshift $z = 7$, showing the mass-weighted temperature along the line of sight (background). Above the curved white line is the THESAN simulation, and below the line is the Uniform UVB simulation. The THESAN simulation shows significantly cooler temperatures in void regions, with these areas remaining neutral. The circle, which is 80 physical kpc in diameter, surrounds the most massive galaxy in the volume, with zooms shown for both simulations. Within the zooms, the HI gas density is shown, with the THESAN simulation exhibiting significantly ($\approx 10\times$) higher HI fractions than the Uniform UVB one.

greater HI gas density in filaments, with a factor ~ 10 lower density in the surrounding CGM.

In the remainder of the paper, we aim to understand the impacts of these two reionization models, and hence different gas phase structures, on the process of galaxy formation by studying in detail the properties of galaxies.

2.1 Simulation Code

The simulations in this paper were performed using AREPO-RT (Kannan et al. 2019), which is based upon the AREPO moving mesh magnetohydrodynamics code (Springel 2011; Pakmor & Springel 2013; Weinberger et al. 2020). They are an extension of the THESAN project (Kannan et al. 2022b; Smith et al. 2022; Garaldi et al. 2022), and use the same physical and numerical models as these simulations. We briefly summarise these models here, and refer in-

terested readers to Section 2 of Kannan et al. (2022b) for a detailed descrpition.

AREPO-RT solves the (radiation-, magneto-) hydrodynamical equations on an unstructured Voronoi mesh, with gas 'particles' acting as mesh-generating points (Pakmor & Springel 2013). This moving mesh solver is quasi-Lagrangian, and solves the hydrodynamic equations in the rest frame of an interface between all mesh generating points, which are regularized frequently (Vogelsberger et al. 2012; Pakmor et al. 2016). Gravitational forces are solved (including periodicity) using a Hybrid Tree-PM approach which employs an oct-tree to solve for short-range forces, with long range forces computed with the particle mesh method (Springel 2005; Springel et al. 2021).

Radiation transport is handled using a moment-based approach, and solves the hyperbolic conservation equations for photon number density and flux using the M1 closure scheme (Levermore 1984; Dubroca & Feugeas 1999). The UV continuum is grouped into three frequency bins with energy intervals $[13.6, 24.6, 54.4, \infty)$ eV, and we use the reduced speed of light $\tilde{c} = 0.2c$ and subcycling (allowing 32 subcycles) of the radiation transport to improve the speed of the calculation. We couple these photons to the gas using a non-equilibrium thermochemistry module that tracks abundances of five species: HI, HII, HeI, HeII, and HeIII. The final cooling rates for gas include contributions from this non-equilibrium thermochemistry (i.e. primordial cooling), equilibrium models for metal cooling following Vogelsberger et al. (2013), and compton cooling. Our metal cooling rates are computed assuming metals are in equilibrium with a spatially-uniform UV background with the radiation field given by a Faucher-Giguère et al. (2009) model, which is potentially problematic given that reionization proceeds differently in our simulations. Unfortunately a full calculation including nonequlibrium metal cooling on the scales studied here is infeasible given present computational restraints, and we are mainly interested in differences between our two reionization models rather than making absolute predictions.

To simulate key processes that occur on scales smaller than those resolved in the simulation, notably star formation, stellar feedback, black hole formation, and AGN feedback, we use the IllustrisTNG galaxy formation model (Marinacci et al. 2018; Naiman et al. 2018; Nelson et al. 2018; Pillepich et al. 2018b; Springel et al. 2018; Pillepich et al. 2019; Nelson et al. 2019b,a), an update to the previous Illustris galaxy formation model (Vogelsberger et al. 2014). We use the sub-resolution treatment of the interstellar medium (ISM) from (Springel & Hernquist 2003), star formation and feedback following (Pillepich et al. 2018a), and AGN formation and accretion following (Weinberger et al. 2017). In addition, we use the empirical dust treatments from McKinnon et al. (2016, 2017), and track dust properties of each gas cell.

Radiation is produced by stars and AGN, though in the volumes studied here the contribution from AGN is negligible as there are only four black holes in our largest volume, with a maximum mass of $M_{\rm BH} \approx 5 \times 10^6$ M$_\odot$. As such, we refer the reader to Kannan et al. (2022b) for a description of our black hole and AGN implementation, and only describe the implementation of stars and their feedback here. The luminosity and spectral energy density of stars in THESAN is given as a complex function of age and metallicity taken from the Binary Population and Spectral Synthesis models (BPASS v2.2.1 Eldridge et al. 2017). The sub-grid escape fraction of stars was set to be $f_{\rm esc} = 0.37$ in the original THESAN simulations to match the global reionization history of the Universe, and we adopt the same value here for consistency.

For the models employing a Uniform UV Background we assume reionization is a near-instantaneous process occurring at redshift $z = 10$ (following the original IllustrisTNG model[1]) with the strength of the radiation field given by the prescription from Faucher-Giguère et al. (2009), as this is a standard practice in cosmological galaxy formation simulations. Simulations with this UVB are performed in the exact same way as the THESAN models, but all sources of radiation have their escape fraction set to $f_{\rm esc} = 0$. The ionizing radiation flux from the UVB is then passed directly to the thermochemistry module, in most cases fully ionizing the gas, though gas can be self-shielded from such radiation if it reaches a high enough density. We employ the model from Rahmati & Schaye (2014) to determine if such gas is self-shielded against the external UVB.

We note here that these new simulations using a Uniform UV background are different than those performed during the original THESAN simulations, for instance THESAN-TNG-2. The prior simulations that used a spatially uniform reionization history and disabled the nonequlibrium thermochemistry module entirely, which leads to small, but systematic, changes in galaxy properties (see Garaldi et al. 2022, Appendix A).

Our simulation models then hence contain all of the typically included physics for a standard galaxy formation simulation (i.e. those targeting $z = 0$, similar to those employed in, for instance, EAGLE, IllustrisTNG, or SIMBA), with the addition of the required physics for reionization (radiative transfer, photon production, and non-equlibrium hydrogen and helium ionisation). We do not include the physics required to accurately track the formation of the first stars (for instance, molecular hydrogen formation, Lyman-Werner radiation, or explicit Population-III star modelling) and the dynamics within mini-haloes. Because of this, we refrain from a full investigation of the initial star formation events, and focus mainly on the differences seen in galaxy populations due to the varying reionization schemes as they pertain to the accuracy of the galaxy formation models.

2.2 Simulation Volumes

Our simulation volumes are generated following a typical Planck Collaboration et al. (2016) cosmology, with $H_0 = 100h$, $h = 0.6774$, $\Omega_{\rm m} = 0.3089$, $\Omega_\Lambda = 0.6911$, $\Omega_{\rm b} = 0.0486$, $\sigma_8 = 0.8159$, and $n_{\rm s} = 0.9667$, with all symbols taking their usual meanings. Gas is assumed to have initially primordial composition with hydrogen mass fraction $X = 0.76$ and helium mass fraction $Y = 1 - X$.

Throughout this paper we use two main simulation boxes, which have co-moving volumes $(4/h)^3$ cMpc^3 and $(8/h)^3$ cMpc^3, named L4N512 and L8N512 respectively. Both volumes contain 512^3 dark matter particles and gas cells initially, giving different mass resolutions (and hence softenings, etc.) for both volumes, as described in Table 1. We note here that all further quantities within this paper are provided h-free, aside from the labels for boxsize denomination. These two volumes were evolved with the two reionization models, a uniform UVB, and the full THESAN model, for four total simulations considered in this paper.

Our simulation volumes are chosen to be small for computational efficiency reasons. Simulating, with radiative transfer, at these resolutions is computationally challenging. Our small volumes hence come with the following important caveats:

[1] We note that the original Illustris and IllustrisTNG simulations used a fixed reionization redshift of $z = 6$, though similar models like EAGLE initiate their UVB at an even higher redshift of $z = 11.5$ (Schaye et al. 2015). We choose here to use $z = 10$ as our fully coupled radiation transport simulations end at $z = 5$ to ensure efficient use of computational resources.

Table 1. Setup information about the two volumes used in this study, along with the main THESAN-1 volume, with information (from left to right) giving: the name of this box within the paper, the total number of particles within the volume, the co-moving box volume, the initial mean mass of gas particles within the simulation, the mass of dark matter particles, and the constant physical gravitational softening used for baryons and dark matter respectively.

Name	Number of Particles	Box Length [cMpc]	$m_{\rm g}$ [$M_\odot$]	$m_{\rm DM}$ [$M_\odot$]	$\epsilon_{\rm g}$ [ckpc]	$\epsilon_{\rm DM}$ [ckpc]
THESAN-1	2×2100^3	95.5	5.82×10^5	3.12×10^6	2.2	2.2
L4N512	2×512^3	5.9	1.13×10^4	6.03×10^4	0.425	0.425
L8N512	2×512^3	11.8	9.04×10^4	4.82×10^5	0.85	0.85

(i) The small volumes are at the mean density of the universe, which on average should be partially reionized by massive external sources. Our volumes, however, will always reionize internally, due to the lack of any external sources. As such, we should expect our volumes to reionize slower on average than a fully representative volume, with the smaller $(4/h)^3$ Mpc^3 volumes reionizing on longer timescales.

(ii) Due to the resolution differences between the volumes, and the cold dark matter model employed, we will see significant differences in the populations of low-mass haloes (i.e. there will be significantly more in the higher resolution, smaller volume, case). As these low-mass haloes may change the topology of reionization, we may not see strong convergence between resolution levels until haloes much more massive than the resolution limit (e.g. > 1000 particles, rather than the typical $32 - 100$ particle limit).

In the top panel of Fig. 2 we show the star formation history of our four simulations alongside the THESAN-1 simulation. THESAN-1 matches well with both of our THESAN volumes, with there being some small offsets in the star formation rate density between models (roughly ~ 0.1 dex, notably not monotonic with resolution; we show in Appendix A the resolution convergence of our results, with the differences here mainly driven by the volume, not resolution). By contrast, the Uniform UVB models show significantly higher (~ 0.3 dex) star formation rates than THESAN before reionization ($z > 10$) that are rapidly damped post-reionization. Our L4N512 volume with the Uniform UVB has a ~ 0.3 dex lower star formation rate than its THESAN counterpart at $z = 9$, shortly after reionization, but by $z = 5.5$, the two reionization models match (aside from differences between volumes). This provides early evidence that the THESAN and Uniform UVB models have broadly acceptable levels of strong convergence at the resolutions studied here ($\sim 10^6$ $M_\odot$ for baryons in THESAN-1, to $\sim 10^4$ $M_\odot$ for our highest resolution THESAN run).

The bottom panel of Fig. 2 shows the mass-weighted HI fraction as a function of redshift. The mass-weighted HI fraction is the total mass of HI gas in the volume divided by the total gas mass in the volume at that epoch. Here we see small differences in the reionization history between the THESAN volumes; as we decrease box-size, we see that the volumes reionize more slowly, with L4N512 reionizing the slowest (at $z = 5.5$, it still has an HI fraction of 20%). This is primarily due to a lack of high mass galaxies ($M_{\rm H} > 10^{11}$ $M_\odot$) which should dominate reionization at late times within this small volume (Yeh et al. 2022). We remind readers that the escape fraction for stars was kept fixed at the value of $f_{\rm esc} = 0.37$ from the main, $(95.5$ cMpc$)^3$, THESAN volume, which was calibrated to match the observed reionization history in that more representative box. As such, we do not expect that these small volumes necessarily match the observed global reionization trends.

All of the THESAN models stand in stark contrast to the Uniform UVB models (the two volumes overlap on this figure) which shows an instantaneous drop in the HI fraction to almost zero at $z_{\rm reion} = 10$, as expected. The only HI gas that can remain at $z < 10$ is gas that is self-shielded, making up a very small fraction of the total gas mass in the volume (and hence an even smaller fraction by volume).

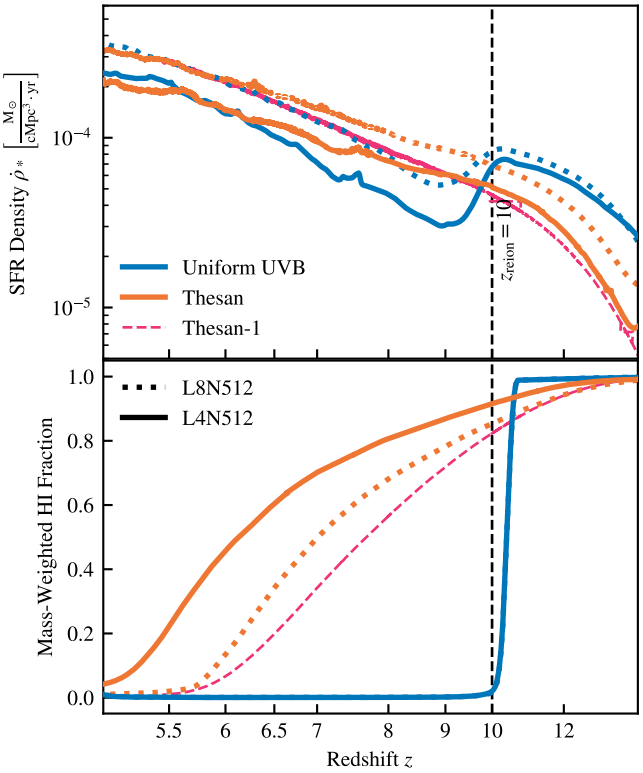


Figure 2. The star formation rate density history of both simulations (top) and the global mass-weighted HI fraction history (bottom). Indicated by the black dashed line is the instantaneous reionization redshift of $z = 10$ in the Uniform UVB model. Pre-reionization, the Uniform UVB model is able to sustain a higher global star formation rate density, due to a lack of photoionization heating from stars. Post-reionization, this star formation rate drops significantly (a factor of ≈ 4) as star forming regions in low-mass galaxies are evaporated by the strong UV background. The THESAN model reionizes much less quickly, fully reionizing the volume (i.e. a HI fraction of approximately zero) around redshift $z = 5.6$. In pink, we show the reionization history of the original THESAN-1 simulation for comparison.

We further demonstrate the evolution of key macroscopic quantities in the multi-panel Fig. 3, which paints an overall picture of a very different IGM between our two reionization models. From top to bottom, we show the mass-weighted gas metal mass fraction, gas projected density, mass-weighted HI fraction, and mass-weighted gas temperature projected through the entire L4N512 volume. Different columns demonstrate these maps at different epochs, and within each panel the top left shows the THESAN volume, and the bottom right the 'mirror image', but for the Uniform UVB model.

The Uniform UVB model takes an early lead in polluting the IGM with metals (at $z = 11$) thanks to increased star formation rates relative to THESAN, but THESAN catches up with both maps matching

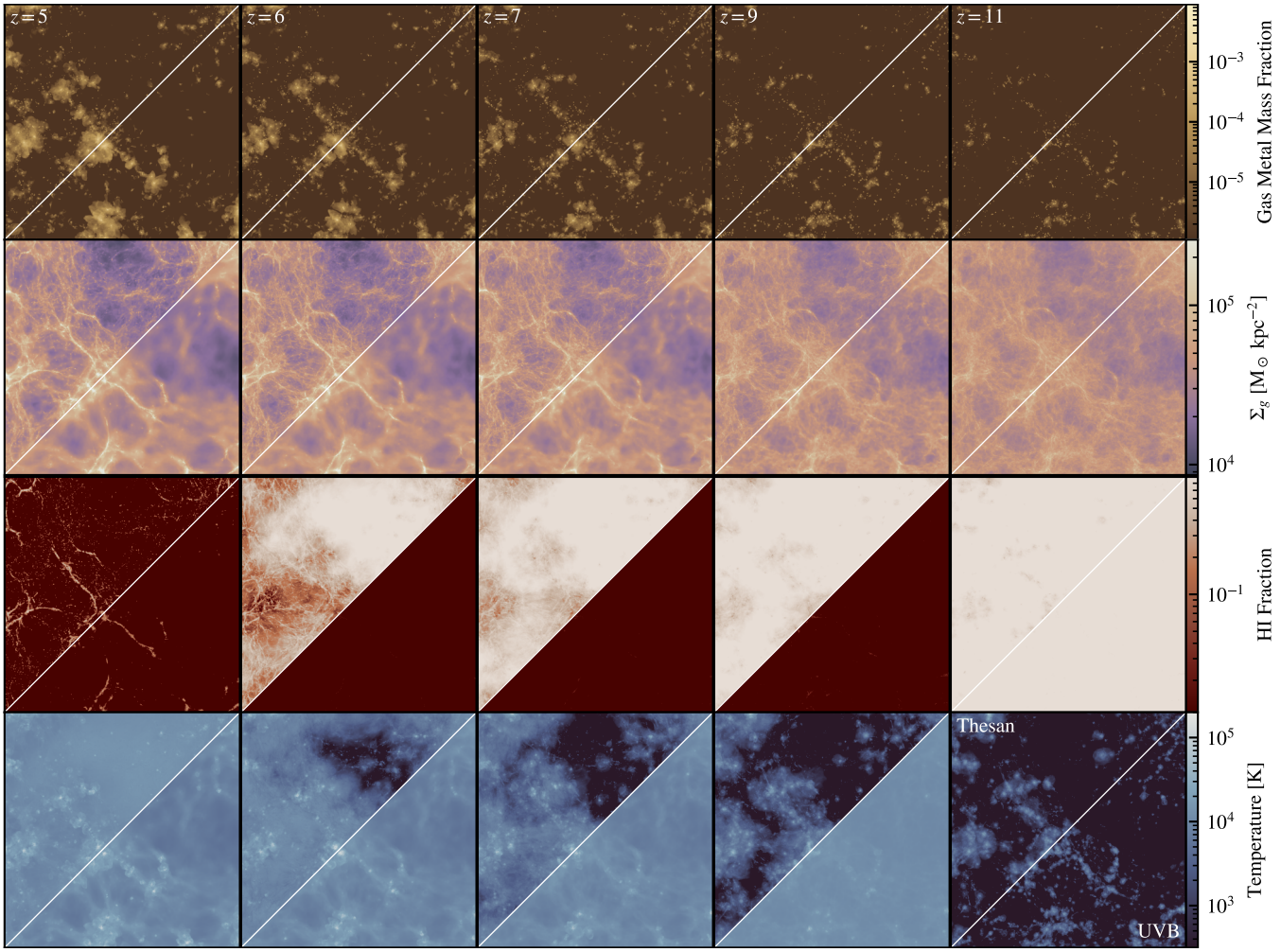


Figure 3. Macroscopic evolution of four key quantities in the L4N512 volume (with the entire volume shown in projection; quantities are calculated as the mass-weighted mean over the line of sight): the gas metal mass fraction, defined as the fraction of mass of each gas cell in the metal phase, the projected gas density Σ_g, the HI gas fraction, and the temperature. The lower right of each panel shows the result from the Uniform UVB simulation, with the upper left showing the same part of the volume (mirrored) but in the THESAN simulation.

well at $z = 5$, albeit with more metal pollution in voids in THESAN. In the second row, we see the main cause for this increased void region pollution; the slower (and weaker) reionization process in THESAN allows dense structures to occur at much smaller spatial scales than in a universe with a Uniform UVB, with filaments much more prominent in the underdense regions that are all but washed out by photoheating from the UVB.

The slow roll of reionization is abundantly clear in the third row of figures showing the HI fraction as a function of time. In THESAN, the void in the top of the panel does not fully reionize until $z \approx 5.5$, leaving a vast majority of the volume neutral until this time. In addition, we see a large abundance of self-shielded regions remain even at $z = 5$ in this underdense region, as well as there being strong self-shielding amongst the filamentary structure. By contrast, the instantaneous reionization in the Uniform UVB model shows a much simpler history, with only a small fraction of self-shielded regions able to form at $z \approx 5$, with there being far fewer self-shielded filaments than in THESAN at this time, and a complete lack of small self-shielded haloes.

The final panel gives the temperature evolution of the universe, which shows the impact of early photoheating from the first galaxies in THESAN. The panel showing $z = 11$, before reionization in the Uniform UVB universe, shows a more extended hot circumgalactic medium (CGM) around THESAN galaxies due to additional radiative feedback (see Fig. 4 in Garaldi et al. 2022). At $z = 9$, however, this trend is reversed as the mean intergalactic medium (IGM) temperature is pushed above $T_0 > 10^4$ K by the strong ionizing radiation field in the Uniform UVB, whilst in THESAN it can remain below 10^4 K until $z < 7$, even in the full THESAN-1 volume with orders of magnitude more massive (and hence bright) galaxies (Kannan et al. 2022b).

In Fig. 4 we consider the phase space evolution of the two L4N512 simulations. The top row shows the relationship between gas density and temperature, coloured by the metal mass fraction of the gas, for the Uniform UVB simulation. The bottom row shows the same, but for the THESAN simulation.

The early lead in metal pollution that we saw in the top panels of Fig. 3 is confirmed here, with low-density ($n_H \approx 10^{-4}$ cm^{-3}) hot ($T > 10^4$ K) gas having a higher metal mass fraction at $z = 11$.

The signature of the instantaneous reionization of the Uniform UVB model is again clear, with primordial gas heated to $T \gtrsim 10^4$ K at $z = 10$, a process that is not fully repeated in THESAN even at $z =$

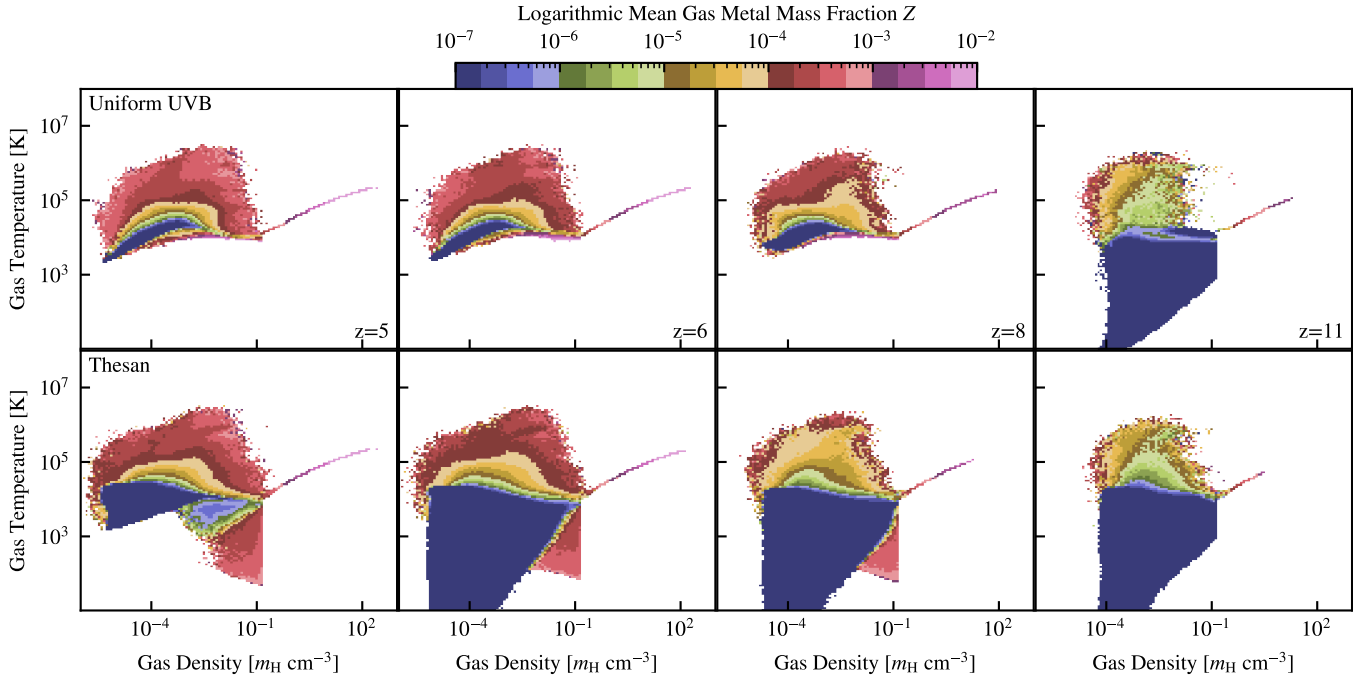


Figure 4. Phase-space diagrams, showing the temperature and physical density distribution of gas in the L4N512 simulations (rows), at various redshifts (columns). Pixels are coloured by the mean metal mass fraction (Z) in the bin, which is averaged logarithmically (i.e. $Z = \exp \mathrm{mean}_i \log Z_i$, where i is the particle index), with white pixels containing zero gas cells. Notable is the presence of cold, low density, gas at redshifts $z > 10$ for both models, which is removed instantaneously at $z = 10$ by the reionization model in the Uniform UVB simulation. This cold, neutral, gas remains in the THESAN simulation until the entire volume reionizes (approximately $z = 5.6$).

5. THESAN has a population of intermediate metallicity $Z \approx 10^{-4}$ gas at $T < 10^3$ K and high density (i.e. self-shielded HI gas) even down to $z = 5$, a component that does not exist in the Uniform UVB simulation.

In both cases the ISM ($n_\mathrm{H} > 10^{-1}$ cm^{-3}) evolves similarly, though it extends to higher densities early on in the Uniform UVB model due to the lack of photoheating feedback from early stars. This is expected as we use the equilibrium model from Springel & Hernquist (2003) for our ISM for consistency with THESAN and other large-volume cosmological simulation suites like EAGLE and IllustrisTNG (Schaye et al. 2015; Pillepich et al. 2018a).

In summary, these first visualisations show how the IGM, CGM, and ISM evolve differently on a global scale within the two reionization models. THESAN allows colder, self-shielded, and metal-poor gas to exist to significantly later times than the Uniform UVB model, and this will undoubtedly have a back-reaction on galaxy evolution.

3 IMPACT ON GALAXY PROPERTIES

The chosen reionization model only interacts directly with the gas phase, but this may then back-react on both the stellar phase and dark sector. In this section we explore the impacts of the chosen reionization model on the properties of galaxies within the simulation, in an effort to further understand this back-reaction on the whole population.

In Fig. 5, we show the stellar mass function of galaxies over time in both simulations. The top panel gives the mass function in the L8N512 volume, with the bottom panel showing the same but for the L4N512 volume. In both cases we see that low-mass substructures ($M_* < 10^6$ M$_\odot$) are significantly suppressed in the Uniform UVB model, with there being as much as a ~ 0.5 dex difference relative to THESAN. This difference persists even to low redshift, as these low mass galaxies typically have formed early (and cannot form at later times, as the THESAN volume fully reionizes).

At the highest masses, $M_* > 10^7$ M$_\odot$, both models predict a similar abundance of galaxies, with even small-scale box-dependent structure in the SMF being preserved (e.g. the kink at $M_* \approx 10^{6.5}$ M$_\odot$ in the L8N512 volume at $z = 6$), indicating that high-mass galaxies may evolve similarly between the two simulations. This is expected, as these galaxies have grown mainly in an era where they have reionized themselves (inside-out reionization), giving results similar to the fully ionized case.

For comparison purposes, we show extrapolated Schechter fits from four observational data collections, collated in Bhatawdekar et al. (2019). All fits here are extreme extrapolations, as the lowest mass galaxies traced by these observations in the Hubble Frontier Fields, Hubble Ultra Deep Field, and CANDELS surveys are around $M_* \sim 10^7$ M$_\odot$ (thanks to gravitational lensing of background galaxies), roughly corresponding to the *highest* mass galaxies in the model. We generally show a good match to the most recent observations from Song et al. (2016) and Bhatawdekar et al. (2019), matching with the fits well down to $M_* \sim 10^5$ M$_\odot$ for the THESAN models (with there being an under-abundance of galaxies of this mass in the UVB models).

Earlier data from Duncan et al. (2014) significantly overshoots our models, though this data uses just the CANDELS South field (Guo et al. 2013) and is complete only down to $M_* \sim 10^9$ M$_\odot$, leaving a lot of freedom in the low-mass end of the fit (with a relative 1σ error of 50% in the low-end slope α, where newer observations have constrained this to within 10%). Additional early data from Grazian et al. (2015) significantly undershoots our models, but again was complete only down to $M_* \sim 10^9$ M$_\odot$, and provides a low-end slope

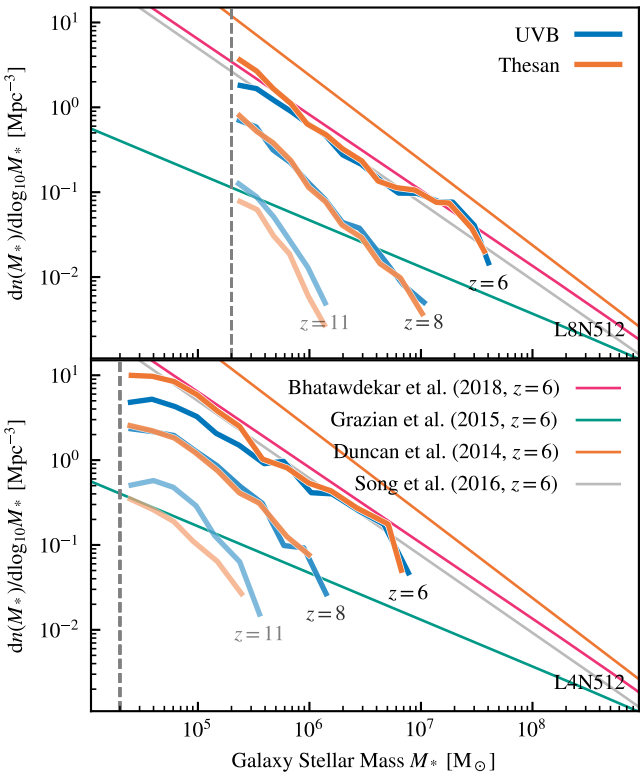


Figure 5. Galaxy stellar mass function in both simulation boxes (L8N512 in the top panel, L4N512 in the bottom panel), for both models (Uniform UVB shown in blue, and THESAN shown in orange). THESAN shows a much higher abundance (~ 0.5 dex) of low mass ($M_* < 10^{6.5}$ M$_\odot$) galaxies. The vertical grey line shows the mass of a single star particle in both models. Various line transparencies show the evolution with redshift, with the corresponding redshifts noted next to the lines at the same level of transparency. Vertical offsets of 0, -0.5, and -1 dex are applied at redshifts $z = 6$, 8, and 11 respectively for clarity. In the background, we show fits to data from Duncan et al. (2014); Grazian et al. (2015); Song et al. (2016); and Bhatawdekar et al. (2019).

that is in tension with the more recent observations of Song et al. (2016) and Bhatawdekar et al. (2019).

Given that the TNG model parameters were tuned to fit low-redshift ($z \sim 0.1$) data (Pillepich et al. 2018a), this level of agreement at high redshift and high resolution when the full THESAN reionization model is included is remarkable. Future observations (and associated modelling) from upcoming *JWST* surveys, including *JADES*, will allow for even tighter constraints on the abundances of galaxies at high redshift.

In Fig. 6 we show the UV luminosity function (UVLF), which shows the abundance of galaxies as a function of their UV luminosity at 1500 Å (here denoted as M_{1500}). These magnitudes are generated as in Smith et al. (2022), using the Binary Population and Spectral Synthesis code (BPASS version 2.2.1 Eldridge et al. 2017). A correction is then applied for galaxies with poor sampling of their star formation histories (see Section 3 of Smith et al. 2022).

The figure here is laid out similarly to the stellar mass function in Fig. 5, with the top panel showing the UVLF for the L8N512 volume, and the lower panel for the L4N512. We seen an even larger discrepancy between the volumes simulated with the full THESAN model and the Uniform UVB models, with there being a factor ~ 1 dex difference in abundance of galaxies with $M_{1500} \approx -8$. These extremely low brightness galaxies are unlikely to be immediately observable, even with *JWST*, though there is some hope that their abundances may be understood in lensing fields. Following Jaacks et al. (2019), we show we show the approximate absolute UV magnitude limits for *JWST*, assuming a limiting M_{1500} magnitude of $M_{1500} \approx 32$, which is $M_{1500} \approx -11$ at $z = 6$.

Similarly to the stellar mass functions, the brightest galaxies have almost equal abundances between the two models, likely due to the fact that they reionized internally. We show excellent agreement with observational data from Bouwens et al. (2017) at $z = 6$, and the extrapolated no-turnover model from Atek et al. (2018). There is corresponding agreement with the well-known observations from Livermore et al. (2017) and Ishigaki et al. (2018), though these are omitted from these figures for clarity at $z = 6$. Our THESAN models exhibit significantly less of a turnover at $M_{1500} \approx -13$, as expected from HST lensing fields, with our Uniform UVB models showing some level of turnover. This suggests that there may be significant differences between fields at these low magnitudes simply due to differences in reionization history. Fields that reionized quickly as they host a massive galaxy are likely to prefer a UVLF with a turnover (i.e. galaxy formation in very low mass haloes is suppressed), but those in isolated regions hosting only low mass galaxies that remain shielded will have high abundances of low-mass, and hence faint mini-haloes and protogalaxies. The THESAN and UVB models clearly show significantly larger discrepancies in their UVLFs than their SMFs, a consequence of their different star formation histories. These differences will be explored further in Section 4.

We also show comparisons to two recent simulations: CoDa II (Ocvirk et al. 2020), and SPHINX-20 (Rosdahl et al. 2022). SPHINX provides a comparable luminosity function to THESAN, with it showing no significant turnover at low luminosity[2]. The results from CoDa II do show significant turnover at $M_{1500} \approx -11$, with this suppression being dependent (as in THESAN) on the ionizing radiation background. At these low magnitudes, CoDa II struggles to resolve haloes, with its minimal resolved halo mass $M_H \approx 10^7$ M$_\odot$ having an expected UV luminosity $M_{1500} \approx -8$, meaning this turnover is potentially numerical in origin. CoDa II, due to its fixed grid strategy, also struggles to resolve processes within galaxies, with physical resolution at $z = 6$ larger than 3 kpc. Our L8N512 model, which has similar mass resolution, but better spatial gas resolution due to our adaptive technique, also turns over in all cases around this magnitude, a non-converged effect that goes away as we move to the higher resolution L4N512 volume.

Additionally, the results presented here can be compared with those from the Cosmic Reionization on Computers (CROC) project, specifically the predictions for the faint-end of the UVLF presented in Gnedin (2016b). Both simulation suites, despite using vastly different numerical methods, provide good fits to the available UVLF data. Notably, we both find that the turn-over in the UVLF at faint magnitudes is not reliably predicted by our models, with it being dependent on both the reionization history of the volume (the difference between our orange and blue lines), as well as the specific details of the star formation modeling within the simulations (highlighted here by different turn-over positions at the two different resolution levels).

We explore these trends further in Fig. 7, which shows both the stellar-to-halo mass ratio and subhalo stellar occupation fraction trends with mass for all of our models. We choose to show the total stellar mass bound to the subhalo M_* and total halo mass bound to

[2] The increased abundance of all galaxies at low masses is likely due to higher stellar masses across the board for SPHINX; see the discussion around Fig. 7.

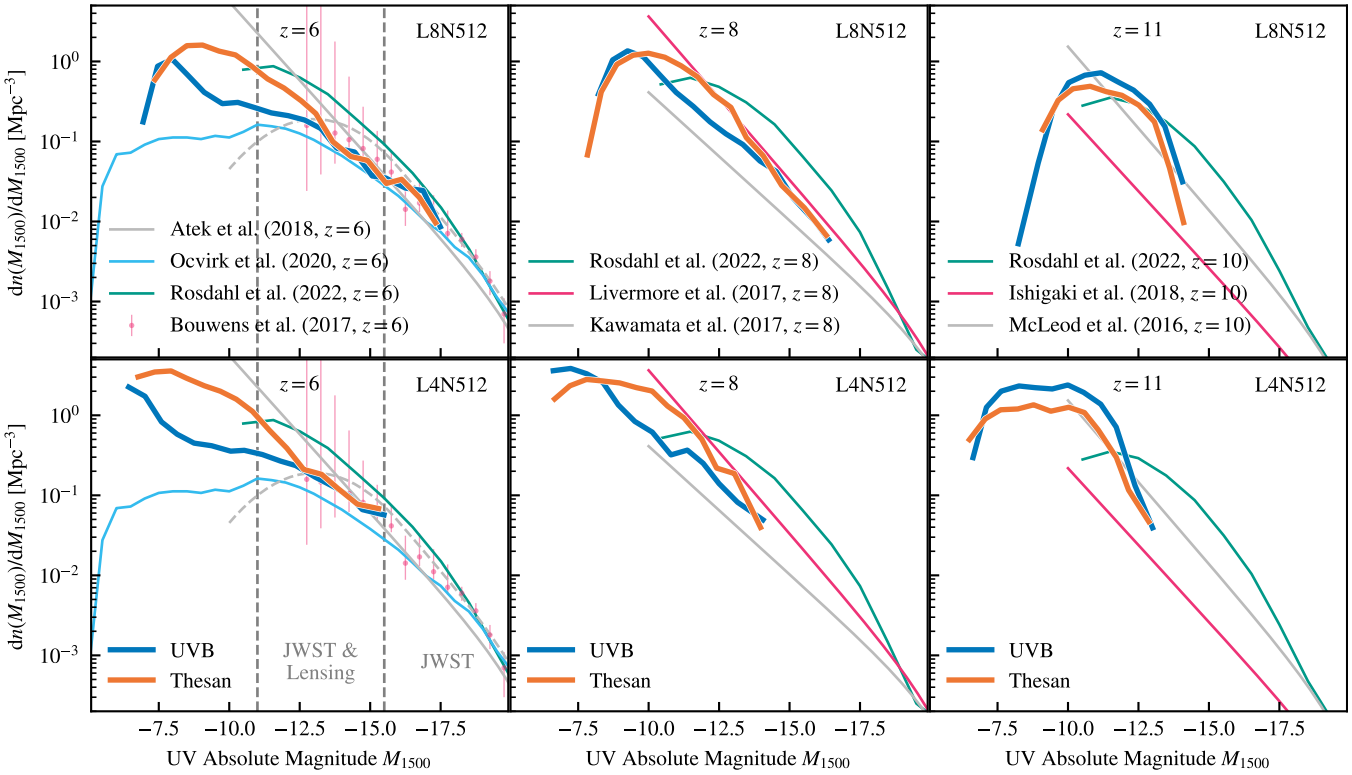


Figure 6. The UV luminosity function (in the rest-frame M_{1500} band) for the two boxes (with L8N512 in the top row and L4N512 in the bottom row), and the two models (Uniform UVB shown in blue, and THESAN shown in orange). Each column shows a different redshift, with the corresponding redshifts at the top of each column. There is a significant under-abundance of galaxies with $M_{1500} < -14$ in the Uniform UVB model which appears to be converged with resolution. In the background, we show comparison observational data from Bouwens et al. (2017) and Atek et al. (2018) (dashed line shows a fit that allows for a low-brightness turn-off, solid includes no such component), and comparison simulation data from Ocvirk et al. (2020) and Rosdahl et al. (2022) at $z = 6$. At $z = 8$ we again show the SPHINX simulation in green, with fits from Livermore et al. (2017) and Kawamata et al. (2018) in pink and grey respectively. Finally, at $z = 11$, we show comparison data at $z = 10$ (we choose to show $z = 11$ from the simulation to ensure a pre-reionization state in the UVB model) from SPHINX, and fits to data from Ishigaki et al. (2018) and McLeod et al. (2016) in pink and grey respectively.

the subhalo $M_{\rm H}$ here, for more straightforward comparisons (Rosdahl et al. 2022), a departure from the main THESAN papers. All subhaloes are shown in the background as appropriately coloured scatter.

Similarly to our abundances, we see that the stellar-to-halo mass ratio $M_*/M_{\rm H}$ is well converged between simulation resolutions and even reionization models at all redshifts for masses $M_{\rm H} \gtrapprox 10^9$ M$_\odot$. As in Kannan et al. (2022b) our models match well with the abundance matching results from UNIVERSEMACHINE (Behroozi et al. 2019) at all valid redshifts ($z < 10$). Our haloes are generally in the regime where the UNIVERSEMACHINE fits must be extrapolated, as their fits are only valid down to $M_{\rm H} > 10^{10.5}$ M$_\odot$ (indicated by the dashed part of the pink line in the figure). Our galaxies also match well with the zoom simulations of Pallottini et al. (2022) at $z = 8$, though their lowest mass haloes typically correspond to the highest masses that are available even in our lower resolution L8N512 volume. We find, consistent with the CROC simulation suite, an increasing stellar-to-halo mass relation with time (Zhu et al. 2020). This is consistent with the simple model results from Tacchella et al. (2018), which relied on an assumption that star formation is delayed relative to gas in-fall.

At $z = 11$ we show the fit from Chen et al. (2014) (at $z = 15$ from the Rarepeak simulations), which was shown to match well with extrapolated data from Behroozi et al. (2013). At these very early epochs, the data from Chen et al. (2014) does match well with our background scatter, but we cannot achieve the high levels (1%) of star formation efficiency at halo masses of $M_{\rm H} \approx 10^9$ M$_\odot$ that they find. Using the same model and at the same redshift of $z = 15$, we show the results from O'Shea et al. (2015), which again shows very high star formation efficiencies, meaning that differences here are likely both resolution and model-dependent.

Finally, at $z = 6$, we compare to the results from the SPHINX-20 volume (Rosdahl et al. 2022). We find stellar masses roughly an order of magnitude lower than theirs that are in tension with the aforementioned observational and prior simulation work due to significantly higher star formation efficiencies. Such differences are expected given that the SPHINX model was designed to simulate galaxies at redshifts $z > 5$, and when it is used to trace galaxies to lower redshifts ($z \approx 3$) it has been shown to produce bulge-dominated galaxies Mitchell et al. (2021), whereas THESAN uses the IllustrisTNG model which was calibrated against the stellar-to-halo mass ratio at $z = 0$ (Pillepich et al. 2018a).

Our results for the UVLF and SMF can also be compared to Wu et al. (2019) who also employed AREPO-RT, though with the Illustris galaxy formation model (Vogelsberger et al. 2014), a predecessor to our IllustrisTNG model. Our galaxy stellar mass functions appear broadly similar, and our high-luminosity UVLFs both show excellent agreement with the Bouwens et al. (2017) data at $z = 6$. Wu et al. (2019) did not simulate to a high enough resolution to model galaxies with $M_* < 10^6$ M$_\odot$ (cutting off their UVLF at $M_{1500} = -15$) and as such found that the UVB and fully self-consistent reionization

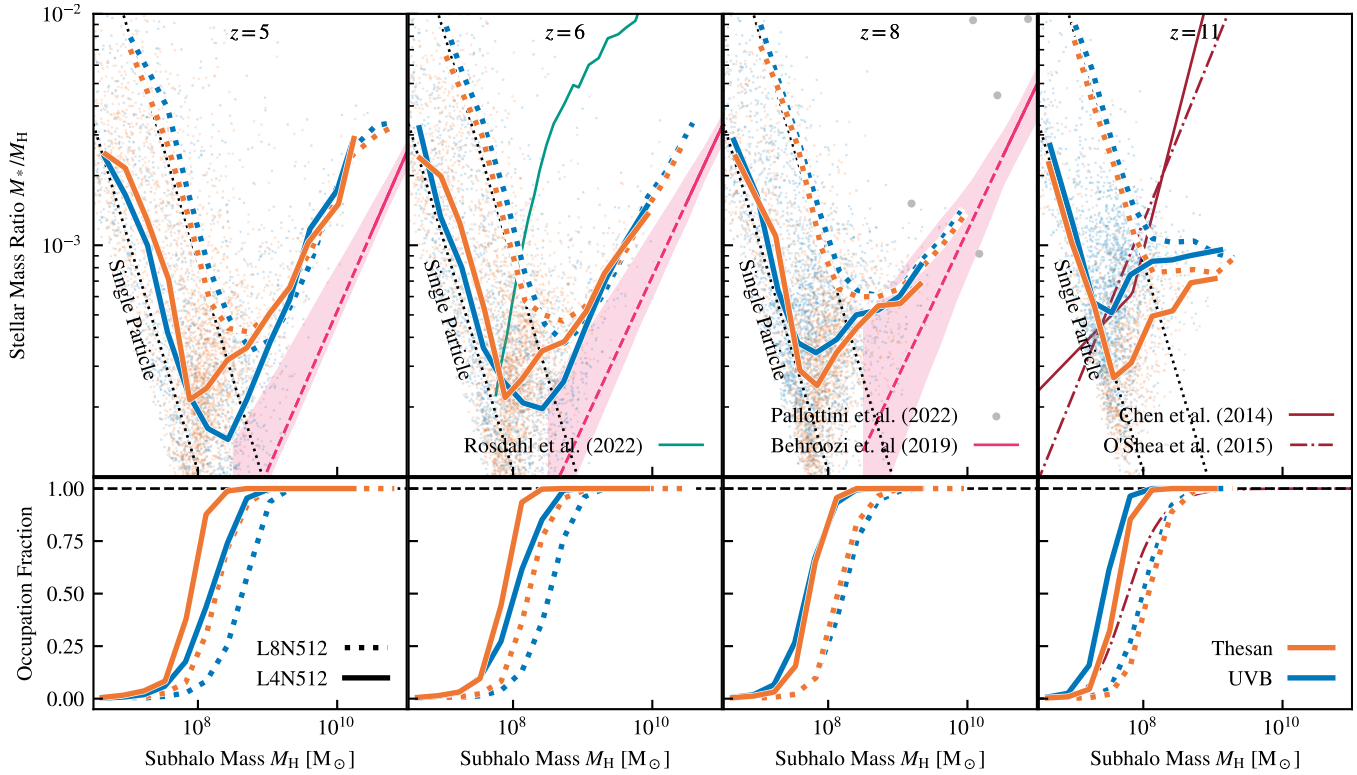


Figure 7. The evolution of the stellar mass-halo mass ratio, across cosmic time (different panels, top row) for each model (differently coloured lines for THESAN and UVB, different line styles for different volumes, refer to the caption). The black dotted lines show the stellar mass ratio for a single stellar particle in the given halo for the two models (L8N512 on top, L4N512 for the lower dotted line). In the background, in the corresponding colours, we highlight the scatter in these relationships for the L4N512 volume. All models are convergent at high masses ($M_H > 10^{10}$ M$_\odot$), but show significant differences at low masses, with notably the L4N512 volume showing a ~ 0.3 dex difference in M_*/M_H at $M_H \approx 10^9$ M$_\odot$. We also show results from Rosdahl et al. (2022) (green line, $z = 6$), Pallottini et al. (2022) (grey points, $z = 8$), Chen et al. (2014) (red solid line, $z = 11$), O'Shea et al. (2015) (red dot-dash line, $z = 11$), and Behroozi et al. (2019) (pink line and shaded region; dashed line shows where fits are extrapolated due to minimal mass of $10^{10.5}$ M$_\odot$ in this work). The lower panels highlight differences in occupation fraction, defined as the fraction of haloes within the bin that host at least a single star particle, as a function of halo mass. Though the occupation fraction does not display convergence with simulation resolution, we do see that the THESAN model predicts higher occupation fractions at lower halo masses than the Uniform UVB model.

models were similar on these metrics, whereas we have expanded the parameter space to include lower mass galaxies in our analysis.

Differences between reionization models are largest in the highest resolution volume, which is able to well resolve star formation in haloes with mass $10^{7.5} < M_\mathrm{H}/\mathrm{M}_\odot < 10^9$. The THESAN models have significantly (a factor ~ 2 at $z \approx 5$) higher stellar-to-halo mass ratios in these haloes, indicating a higher star formation efficiency. This is also seen to a much reduced extent in the L8N512 volume, where modelling the star formation histories is limited by poor sampling (the dotted black lines indicate when a single stellar particle resolves the star formation history of the entire halo). The upturn in efficiency at this mass scale is not physical, but numerical in nature, which is clear when comparing results from the L8N512 and L4N512 volumes.

In the lower panels, we show the (stellar) occupation fraction of the haloes. This is calculated as the fraction of haloes within a given M_H bin that host at least one star particle. There is a clear resolution-dependent trend here, indicated best at $z = 11$, where the higher resolution (L4N512) simulations can host star particles at lower halo masses than the lower resolution volumes (L8N512). As the simulation evolves, however, we see reionization-dependent behavior; the THESAN models always host star particles at lower halo masses than their Uniform UVB counterparts at low redshifts ($z < 6$), further indicating that the Uniform UVB models suppress star formation in low mass haloes ($M_\mathrm{H} < 10^9$ M$_\odot$). We see relatively good agreement for our two models with the occupation fractions reported by O'Shea et al. (2015), with both of us reporting no stars in haloes with virial masses $M_\mathrm{H} \lesssim 10^7$ M$_\odot$.

To further investigate the suppression effects of the Uniform UVB model, we show the baryon mass ratio $M_\mathrm{b}/M_\mathrm{H} = (M_* + M_\mathrm{g})/M_\mathrm{H}$ in Fig. 8. As this is (generally) dominated by the gas in the haloes, with $M_\mathrm{b} \approx M_\mathrm{g} \gg M_*$, it is less sensitive to the specifics of star formation physics (though, as seen in Chen et al. (2014), the large scatter in this metric is generally driven by supernova physics).

At early times, all of our models provide consistent baryon mass ratios, with both high resolution and low resolution models hosting the universal baryon fraction $f_\mathrm{b,U} = \Omega_b/\Omega_m = 0.157$ (dashed black line) at halo masses $M_\mathrm{H} < 10^8$ M$_\odot$, and higher-mass haloes hosting slightly lower baryon fractions due to long cooling times and gas pressure.

By $z = 8$, we see the impact of the Uniform UVB model on the gas fractions. THESAN haloes at $M_H < 10^9$ M$_\odot$ can still retain gas to maintain $f_\mathrm{b,U}$, but haloes in the Uniform UVB model have their baryons almost entirely removed as the gas becomes unbound due to external photoheating. This halo mass corresponds roughly to the mass at which haloes have a virial temperature,

$$T_\mathrm{vir} = \frac{1}{2}\frac{\mu m_\mathrm{p}}{k_\mathrm{B}}\frac{GM_\mathrm{vir}}{r_\mathrm{vir}} \quad (1)$$

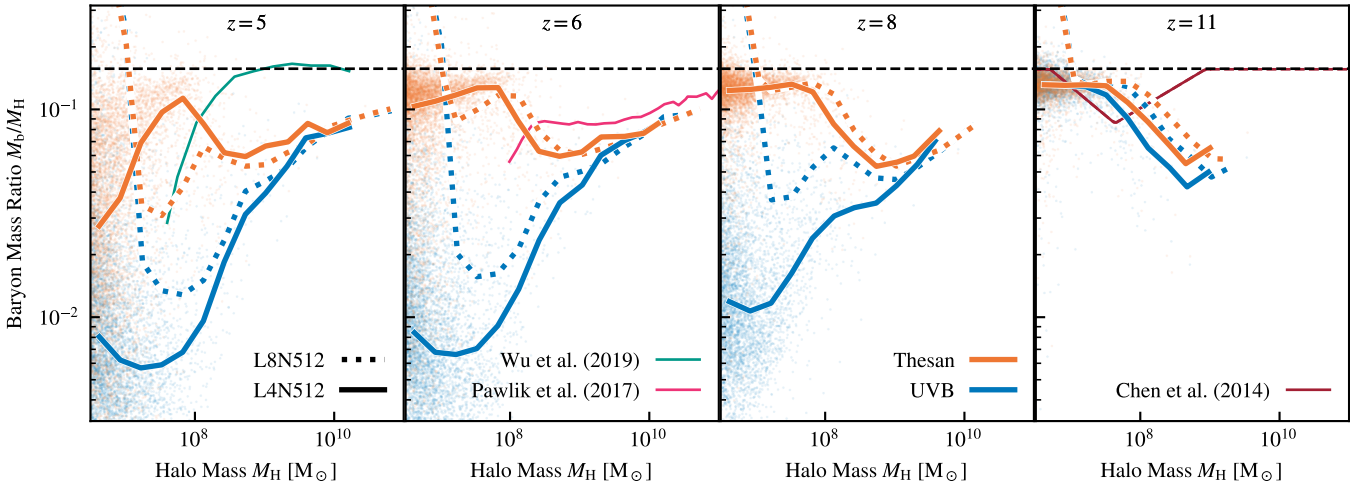


Figure 8. The evolution of the bound baryon mass-halo mass ratio, across cosmic time (different panels) for each model and volume size (differently coloured lines showing the median trend for the two reionization models, with different thick lines showing the different volumes). The dashed line shows the universal baryon fraction, corresponding to $\Omega_b/\Omega_m = 0.157$. In the background, the appropriately coloured points show the scatter in the relation for the L4N512 volumes (each point represents a single subhalo). We see that the Uniform UVB models rapidly lose baryons post-reionization in low mass haloes ($M_H < 10^9$ M$_\odot$), with the THESAN volumes retaining close to the universal baryon fraction even down to $z \approx 5$. In the background, we show results from Pawlik et al. (2017) (pink line, Aurora, L12N512, $z = 6$), Chen et al. (2014) (red line, $z = 11$), and Wu et al. (2019) (green line, $z = 5$, Illustris model) and see good agreement between these results and the THESAN models.

where μ is the molecular weight per particle for fully ionized gas, m_p the proton mass, k_B the Boltzmann constant, G is Newton's gravitational constant, and M_{vir} and r_{vir} are the virial mass and radius of the halo, of around 10^4 K. Hence fully ionized hydrogen gas in thermal equilibrium has enough thermal energy to escape the gravitational potential and becomes unbound to these low mass haloes.

As haloes of these low masses are slowly externally reionized, the THESAN models see a reduction in the baryon fraction at low masses all the way down to $z = 5$. As previously discussed, at $z = 5$ there is still a small fraction of our L4N512 ($x_{HI} \approx 0.05$) and L8N512 ($x_{HI} < 0.01$) volumes that are neutral, meaning that the baryon fractions still do not match the Uniform UVB models at this time. There is significant down-scatter from the universal baryon fraction in the THESAN model here, with this spread representing haloes that are in the process of being externally reionized.

At $z = 6$ we are able to compare with prior simulation results from the Aurora simulations presented in Pawlik et al. (2017). We match well, to within 0.1 dex for our medians at high masses. The Aurora simulations do not have the resolution (their highest resolution volume would be L12N512 in our parlance) to fully capture the transition to haloes with virial temperatures lower than 10^4 K as we do, but they maintain high baryon fractions comparable to our two THESAN models at this redshift.

At $z = 5$ we show the results from Wu et al. (2019), which used the Illustris galaxy formation model. We see broadly similar trends to our own THESAN models, though the Illustris model is able to retain universal baryon fractions at $M_H > 10^{8.5}$ M$_\odot$, despite their use of $f_{esc} = 0.7$, indicating inefficient stellar feedback.

Fig. 9 explores another key galaxy scaling relation: the mass–size relationship. Here we show the mass contained within a spherical aperture of size twice the stellar half-mass radius, with the stellar half-mass radius calculated as the radius of a spherical aperture containing half of the bound stellar mass to each subhalo.

Galaxies at these high redshifts and low masses have small sizes, typically around $R_{1/2,*} \approx 1$ kpc, and have not yet formed disc-like morphologies. We see that the differences in baryonic accretion and retention translate into differences in the stellar morphologies, with THESAN galaxies having sizes typically ~ 0.1 dex larger, consistent with less rapid early star formation and lower levels of bulge formation (Crain et al. 2015). This is true across all epochs post-reionization, with THESAN galaxies still maintaining larger sizes at $z = 11$ due to the additional radiative feedback (Wise & Abel 2008; Wise et al. 2012b).

There are no reliable observations of galaxy sizes of these masses available for comparison, but we do see that our galaxy sizes (at mass scales where the simulations overlap) are consistent with those found in TNG-50 (Pillepich et al. 2019, although those results are only available at $z = 2$ in published work).

Finally we turn to the metallicities of our galaxies. Fig. 10 shows the stellar metal mass fractions (Z_*) of our galaxies as a function of their stellar mass. We see here that the Uniform UVB simulations generally form galaxies with significantly higher metallicities than the THESAN model. This can be connected back to the phase space diagrams in Fig. 4, where we showed that THESAN allows for cold, low metallicity (or even primordial) gas to remain until even $z = 5$, which can accrete easily into galaxies for star formation. We note that the dust content of the galaxies is similar between the two reionization models. Additionally, the low-mass neutral haloes in Fig. 1 can allow for significant ex-situ star formation for even these massive galaxies, with these early stars being extremely metal poor.

We show, for comparison, two models that report stellar metallicities. First, the fit from Chen et al. (2014) shows significantly lower metallicities at low masses than we do, but matches at $M_* \approx 10^7$ M$_\odot$. Chen et al. (2014) uses stellar particle masses that are much lower than ours (in some cases $M_* \approx 10^3$ M$_\odot$), and additionally include a separate model for Pop III stars. This changes their early enrichment behaviour relative to ours. By comparison the FLARES simulations of Wilkins et al. (2022), that target much higher msases, and use a Uniform UVB model, match well with our simulated model employing a Uniform UVB.

In addition to these prior models, we show early *JWST* results from SED fitting from Furtak et al. (2022). These observations are

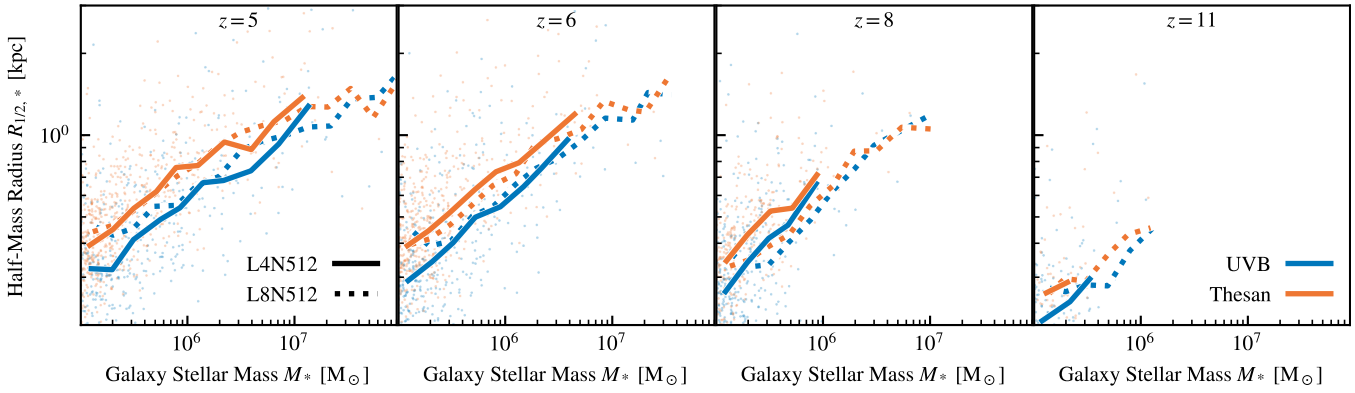


Figure 9. The half-mass stellar sizes of galaxies for both models (line colours) and box-sizes (line styles). Each panel shows a different redshift from $z = 11$ to $z = 5$. Typically the THESAN model leads to stellar sizes that are roughly ~ 2 times as large as the Uniform UVB model, indicating significant differences in galaxy morphology and evolution that are dependent on the reionization history of both the central galaxy and its numerous progenitors.

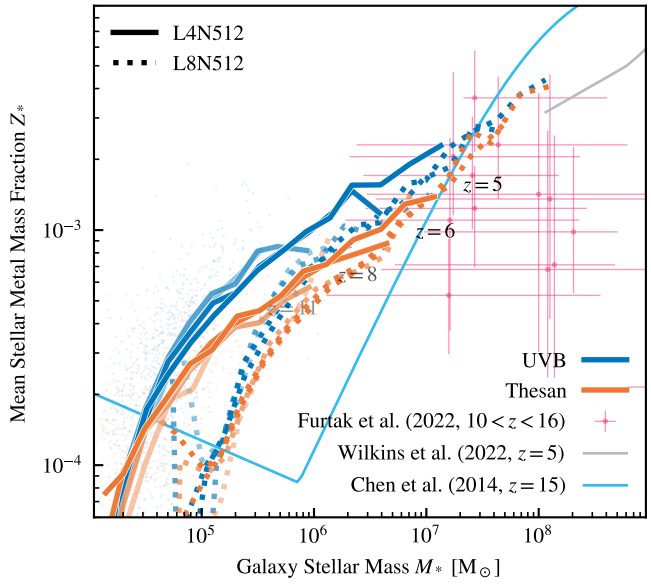


Figure 10. The mean stellar metal mass fraction of stars within galaxies ($R < 2R_{1/2,*}$) as a function of their mass within the same aperture. Solid lines (and background scatter) show the median trend in the higher resolution L4N512 volume, and dotted lines show the lower resolution L8N512 volume. Different transparency levels within lines show different redshifts, with labels appropriately transparent. We see that the Uniform UVB model leads to systematically (~ 0.3 dex) higher stellar metallicities within galaxies, though the L4N512 volume shows a greater degree of separation.

of galaxies lensed behind the cluster SMACS J0723.3-7327 (Atek et al. 2022) using the seven broad-band filters from NIRCam, and one band from NIRISS, with SED fits completed using BEAGLE. Though the error bars are large, and these observations are from only one field, we already see that our Uniform UVB model in our highest resolution simulation overshoots the majority of the data. Our highest resolution THESAN model, that reliably can form self-shielded minihaloes with $T_{\rm vir} < 10^4$ K, and hence fuel galaxies with cold primordial gas and ex-situ metal poor stars, shows a trend that looks to be more consistent with these early observations. Additional observations are available from Tacchella et al. (2022), but the galaxy stellar masses are too high ($M_* > 10^9$ M$_\odot$) for reliable comparison to our small volumes.

4 UNDERSTANDING GAS PHASE EVOLUTION

To better understand this process of primordial gas fueling, we now turn to the gas phase and birth properties of stars. Wise et al. (2014) and Chen et al. (2014) found that galaxies in haloes with virial temperatures $T_{\rm vir} < 10^4$ K dominate early galaxy formation, which appears generally consistent with our prior findings.

In Fig. 11 we show the CGM properties of all central haloes in our simulations. To calculate the CGM properties, we take each central halo, and only include gas that is bound to the central subhalo, with all other subhaloes removed. We then remove gas that is in the central 'galaxy' by excluding gas cells that lie within twice the stellar half-mass radius $R_{1/2,*}$. Filtering spatially rather than by gas properties excludes the vast majority of ISM gas, whilst allowing any recently accreted dense gas in the CGM to remain part of our selection.

The top row of this multi-panel figure shows the evolution of the mass-weighted mean CGM gas temperature with cosmic time. In the background, we show all haloes as appropriately coloured scatter (for the L4N512 volume), and the lines represent the median value binned as a function of halo mass.

At early times ($z = 11$), the median trend closely follows the virial temperature of the host haloes. We see significant up-scatter from the median in the Uniform UVB, due to higher star formation rates in the highest mass haloes and hence stellar feedback that can heat the surrounding CGM.

Post-reionization in the Uniform UVB model we see that all haloes with $M_{200,\rm crit} < 10^{8.5}$ M$_\odot$ have a CGM temperature consistent with the recombination equilibrium temperature for HII gas, as all CGM gas in this model is ionized by the external radiation field. The lowest mass haloes in THESAN, by comparison, retain a cold CGM with $T_{\rm CGM} < 10^4$ K (albeit with more scatter as some photo-heating occurs). This trend occurs until $z = 5$ when the majority of the region (and certainly most CGM) is reionized, where the minimal temperature of CGM gas is $T_{\rm CGM} \approx 10^4$ K. Differences in the $z = 5$ CGM temperatures are also seen, with the UVB heating the gas to a temperature ~ 2 times as high as the THESAN model. This will impact gas accretion rates and the impact preventative feedback even now that the volume is reionized.

We see further evidence of the early star formation boost in the Uniform UVB model through enrichment of the CGM in the second row of Fig. 11. Here we show the mass-weighted mean gas metal mass fraction of the CGM as a function of halo mass, after applying a metallicity floor of 10^{-8}. At $z = 11$ the Uniform UVB model

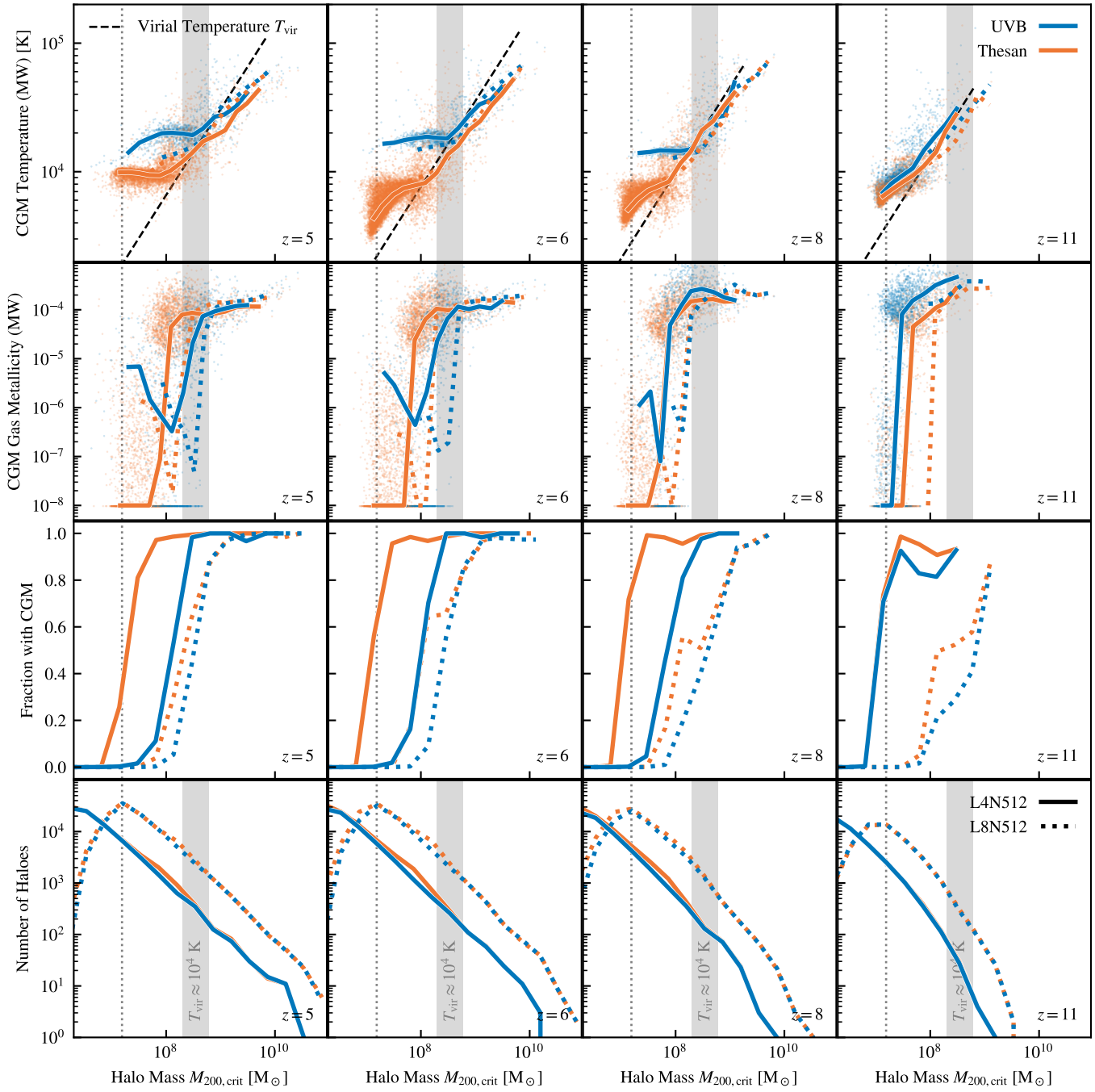


Figure 11. Trends over time of CGM properties (for central haloes only) for the two simulation models (Uniform UVB and THESAN shown as different colours, with the two box sizes and resolutions shown as different line styles, and scatter shown for the L4N512 volume only). *Top panels*: the CGM temperature as a function of halo mass, with the dashed line showing the halo virial temperature according to equation (1). At high redshifts, all simulation models follow this line, but at halo masses corresponding to a virial temperature of lower than $\sim 10^4$ K systematic increases are seen with redshift as the haloes reionize. *Second panels*: the mass-weighted metallicity of CGM gas as a function of halo mass. Post-reionization, haloes with masses corresponding to virial temperatures $T_{\rm vir} < 10^4$ K struggle to retain any primordial gas, as this gas is no longer bound due to its thermal energy. *Third panels*: The fraction of haloes with at least a single bound gass particle in their CGM. Pre-reionization ($z > 10$ in the UVB model), this fraction is close to unity for all resolved haloes (denoted by the dotted line). Post-reionization, no halo with $M_{200,\rm crit} \lessapprox 10^{8.5}$ M$_\odot$ can retain CGM gas. *Bottom panels*: The number of haloes within each mass bin, using the same bins as the above panels. The number of galaxies with CGM included is hence the bottom row multiplied by the third row.

shows stronger enrichment, with ~ 0.5 dex higher CGM metallicities, corresponding to the higher stellar-to-halo mass ratio (Fig. 7). This higher metallicity even persists to $z = 8$, but is washed out by $z = 5$.

At lower masses, $M_{200,\rm crit} < 10^8$ M$_\odot$, the CGM mainly consists of primordial gas. This is crucial, as in strong interstellar radiation fields, it is not possible with $T_{\rm vir} < 10^4$ K to retain gas without metal line cooling. This is made abundantly clear in the transition between $z = 11$ and $z = 8$ in the third row, which shows the fraction of haloes that have a single gas cell bound to their CGM. At $z = 11$, both

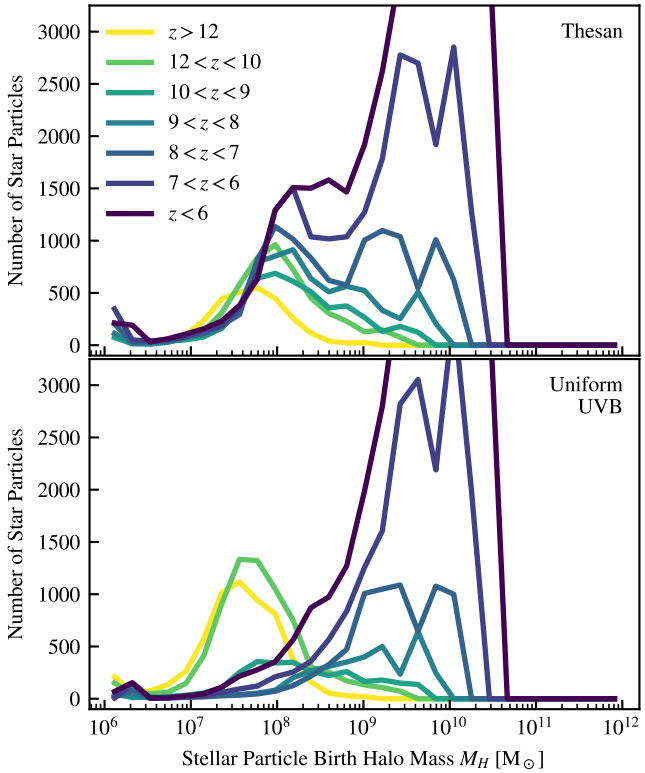


Figure 12. The distribution of birth halo masses, as a function of redshift (differently coloured lines) for the two models in the L4N512 box, with the top panel showing THESAN, and the bottom showing the Uniform UVB model. THESAN can continue to form stars in low mass ($M_H < 10^{8.5}$ M$_\odot$) haloes even down to $z < 6$.

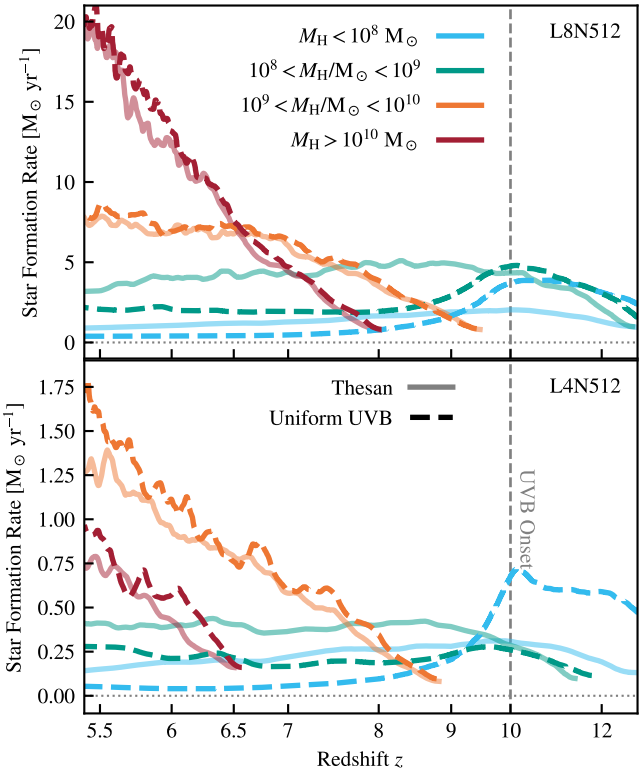


Figure 13. Star formation history, split by the birth halo mass of the stars, for the two box-sizes (top and bottom) and two models (line styles). The vertical dashed line indicates $z = 10$, when the instantaneous Uniform UVB begins. This star formation history was created by using the birth times of the stellar particles, rather than gas star formation rates, and each point is sampled using the birth times of the nearest (in time) 1024 star particles.

THESAN and the Uniform UVB models have bound CGM down to $M_{200,\mathrm{crit}} \approx 10^7$ M$_\odot$, but this CGM is removed at $z = 8$ for the Uniform UVB at masses $M_{200,\mathrm{crit}} < 10^8$ K as photoheating causes gas to become unbound. This is despite there being a large number of haloes within each bin here (over 10^3), showing the spatially universal power of a Uniform UVB.

This story could potentially be changed by significant pre-enrichment from early Pop III stars in molecular cooling haloes not yet experiencing strong Lyman-Werner radiation that prevents the formation of molecular hydrogen, which would allow metal cooling in these low mass haloes to potentially overcome even the Uniform UVB (Wise 2019). This enrichment would need to be significant, however, as at metallicities well below solar $Z \ll Z_\odot$, primordial cooling typically dominates around $T \approx 10^4$ K (Ploeckinger & Schaye 2020). We can see the impact of slow enrichment on these low mass galaxies through the background scatter up from primordial gas in the metallicity of gas in these haloes of $M_{200,\mathrm{crit}} < 10^8$ M$_\odot$ from $z = 8$ to $z = 5$.

In Fig. 12 we show how these different gas phase trends with halo mass can impact the birth of stars in galaxies. For each stellar particle, representing a whole stellar population, we compute both the time of its birth (and hence redshift), as well as the halo mass within which it was first found. This allows us to view where and when stars were born over cosmic time for both simulations. Fig 12 shows the number of stars born in each halo, with each line representing a different redshift.

First considering the bottom panel, we see that in the Uniform UVB simulation many stars are born in haloes with $10^7 < M_\mathrm{H}/\mathrm{M}_\odot < 10^9$ at redshifts $z > 10$. This is shut down immediately, as predicted by the CGM properties in Fig. 11, at the time of instantaneous reionization of $z = 10$. Comparing at these redshifts with THESAN, we see that far more stars are born in these haloes at high redshifts (a factor of ~ 2 more, consistent with Fig. 2).

By contrast, the THESAN model allows star formation to continue in these low mass haloes all the way down to $z < 6$, though at reduced levels as parts of the volume become fully ionized. The additional star formation in these low mass haloes is offset by there being less star formation (i.e. the number of stars born in each halo, as the number of haloes of a given mass is consistent between reionization models) in high mass haloes due to lower amounts of gas accretion and additoinal photoionizing feedback. These two work together to match the bright end of the UVLF, SMF, and global star formation rate at $z \approx 5$ between both THESAN and the Uniform UVB model.

Fig. 13 rephrases the information in Fig. 12 to show the star formation history of the entire volume, but split by birth halo mass. We show the L8N512 volume in the top panel, and the L4N512 volume in the lower panel. The THESAN volumes are shown as solid lines, with the Uniform UVB models shown as dashed lines. The highest mass haloes, with $M_\mathrm{H} > 10^9$ M$_\odot$ have *in-situ* star formation rates that are insensitive to the choice of reioniozation model. These galaxies will have strong enough photoionization fields originating from their own star particles that they effectively live in completely ionized bubbles (aside from self-shielded gas) of their own making, meaning that we do not expect differences between models. However, should a galaxy of this mass have a significant portion of its stars formed ex-situ in lower mass haloes, it will have an altered star formation history.

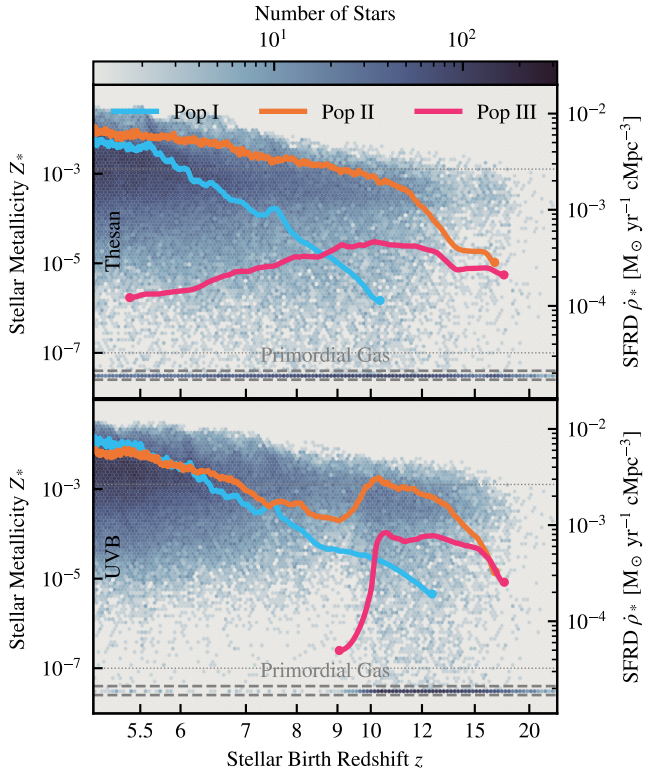


Figure 14. The distribution of stellar metallicities as a function of the birth redshift of the stars (background hexbins, coloured by the number of stars in each bin). The dashed grey lines show purely primordial gas which is given a minimal metal mass fraction $Z_* = 10^{-7.5}$. The secondary axis shows the global star formation rate density $\dot{\rho}_*$, split by stellar epoch (differently coloured lines; dotted grey lines show the metallicity thresholds). The two panels show the THESAN and UVB models (from top to bottom), which both have very different metallicity distributions (Uniform UVB shows almost no low-metallicity Pop III stars below $z = 10$), leading to significant (over ~ 2 dex in Pop II) differences in star formation rates.

For the lower mass haloes, $M_{\rm H} < 10^9$ M$_\odot$, the Uniform UVB model here shows again its higher star formation rate at $z > 10$, before reionization, which is almost completely shut down at that time. THESAN continues forming stars in these low mass haloes at a roughly constant rate until $z = 5.5$, at which time star formation in haloes of $M_{\rm H} < 10^8$ M$_\odot$ is slowly shut down as they succumb to the strong interstellar radiation field. Notably, haloes with $10^8 < M_{\rm H}/{\rm M}_\odot < 10^9$ do not show such a strong reduction in their global (roughly constant) star formation rates, as shown in Fig. 12.

These drastic differences in star formation in low mass haloes also change the types of stars that are born, as stars are created in very different environments. Fig. 14 shows the metallicities of all stars as a function of time for our two models. Stars have been given a minimal metallicity of $Z_* = 10^{-7.5}$, though almost all gas particles below this threshold are fully primordial and are labeled as such.

All star formation in primordial and low metallicity ($Z_* \lessapprox 10^{-6}$) gas is shut down at the onset of the Uniform UVB at $z = 10$. At the same time, there is increased star formation before this time in high metallicity gas (which has been enriched by this first generation of stars). By contrast, the THESAN model shows continual low metallicity, and primordial, star formation across cosmic time down to the end of the simulation at $z = 5$.

Overplotted is an extremely simplistic stellar population model. Pop III stars are chosen as those that have metal mass fraction $Z_* < 10^{-7}$, and Pop II stars have $10^{-7} < Z_* < 0.1 Z_\odot$, where here we take $Z_\odot = 0.134$. All other stars are classified as Pop I stars. We note that here we assign the entire stellar particle (and hence population) to each category, which is certainly an overestimation for Pop III stars. For instance, Jaacks et al. (2018) only assign the first 500 M$_\odot$ of each star particle to Pop III, suggesting that the first star formation event sampled within the entire population would likely enrich neighbouring gas, preventing Pop III formation (see also Smith et al. 2015). We also do not model such stars in-situ, and hence do not apply IMF corrections and the associated differences to feedback efficiency. Nevertheless, it is useful to bin these stars into the various categories to consider potential differences that various reionization models can create.

We see that our Pop III star formation rates are roughly ~ 0.5 dex higher in the Uniform UVB simulation at high redshift, before reionization, but that these drop to zero (implying no more conversion of primordial gas to stars) at that time. THESAN, by contrast, can continue forming these stars down to $z = 5$ (the end of the line is due to a lack of sampling points at later times, not because of the end of Pop III star formation). This is consistent with results from Xu et al. (2016) who also find that Pop III star formation can continue in low mass ($M_{\rm H} \sim 10^8$ M$_\odot$) haloes until late times ($z \sim 7$ in their simulations). Wise et al. (2012b) and Sarmento & Scannapieco (2022) also find that Pop III star formation should continue until late times at a consistent rate of 10^{-4} M$_\odot$ yr^{-1} cMpc^{-3}, which is ~ 0.5 dex lower than ours (though, as noted above, we overestimate Pop III star formation rates here).

Reionization also impacts the tradeoff between Pop II and Pop I star formation at high redshift, with equivalence between Pop II and Pop III reached at $z \approx 8$, rather than $z \approx 5$, in a universe with a Uniform UVB rather than a full reionization model. These differences hence have a significant potential impact when comparing expected SEDs of high redshift galaxies to those that are observed.

5 CONCLUSIONS

In this paper we have explored two reionization models: a spatially-uniform, but time varying, UV background that is commonly used in cosmological galaxy formation simulations, and a fully self-consistent reionization model employing the AREPO-RT code and the THESAN model. Our two models reionize at different speeds, with the Uniform UVB model reionizing instantaneously at $z = 10$, but THESAN taking down to $z \approx 5$ to have a global mass-weighted HI fraction of ≈ 0. We have used two high resolution volumes, with target baryonic masses of $\sim 10^4$ M$_\odot$ (L4N512), and $\sim 10^5$ M$_\odot$ (L8N512) to investigate the impact of these two different reionization models on galaxy formation in the early universe. We found significant differences at low galaxy masses, with haloes of $M_{\rm H} < 10^9$ M$_\odot$ significantly impacted by the choice of reionization model, whereas the properties of higher-mass galaxies were relatively indifferent to this choice. Specifically, we found that:

- As expected, the Uniform UVB model washes out a significant fraction of the cold, dense, structures at $z > 5$, before the entire volume reionizes with the THESAN model. In Fig. 1 we show the diversity of the IGM at early times that is under-represented in a Uniform UVB model. Both the temperature and density of the IGM show significant differences between both models, as demonstrated in Fig. 3 and Fig. 4.
- Our models were shown to match well with observational constraints on the galaxy stellar mass function from Song et al. (2016) and Bhatawdekar et al. (2019) (Fig. 5). For the UVLF, we showed

that the inclusion of a slower reionization model (i.e. THESAN v.s. a uniform UVB) can change the position of the turnover, with galaxies of a $M_{1500} \sim -10$ having a whole dex higher abundance in a THESAN model at $z = 6$ than in a Uniform UVB model (Fig. 6).

- Differences in the UVLF are caused by differences in both the occupation fraction of galaxies (the fraction of haloes of a given mass containing galaxies) and availability of star forming gas within individual haloes. Haloes of mass $M_{\rm H} \approx 10^8$ M$_\odot$ show significantly higher occupation fractions (and higher stellar-to-halo mass ratios) down to $z = 5$ under the THESAN reionization model (Fig. 7). There are also significant differences in the baryon mass ratio ($M_{\rm b}/M_{\rm H}$, $\sim$ 1 dex at $M_{\rm H} \approx 10^8$ M$_\odot$), indicating that the Uniform UVB is driving gas out of low mass haloes ($M_{\rm H} < 10^9$ M$_\odot$) post-reionization (Fig. 8).
- These differences in abundance of both stars and gas also affect the morphologies of galaxies, with THESAN galaxies $\sim 0.1-0.2$ dex larger in their physical stellar extent (Fig. 9), and a factor ~ 2 lower in stellar metallicity (Fig. 10).
- Fundamentally, the differences in properties of galaxies between reionization models are driven by differences in the behaviour of gas in haloes with virial temperatures $T_{\rm vir} < 10^4$ K ($V_{\rm circ} \approx 30$ km s^{-1}). As gas is photoheated by external radiation fields, it becomes unbound in these haloes, and hence in simulations that allow haloes to be fully self-shielded until late times can allow them to be occupied by gas for much longer (Fig. 11). Notably, this means that such processes will not impact simulations that do not have the resolution to model these haloes (typically those with $m_{\rm b} > 10^6$ M$_\odot$, like EAGLE or TNG-100), but that higher resolution simulations (e.g. the zooms from the FIRE suite, (Ma et al. 2019), or TNG-50 (Pillepich et al. 2019; Nelson et al. 2019b)) are missing an important contribution to the distribution of their overall energy budget.
- Changes in gas occupation lead to differences in star formation, with star formation in haloes $M_{\rm H} < 10^9$ M$_\odot$ shut off post-reionization. THESAN allows haloes of this mass to form stars until the entire volume reionizes, one of the major causes of the different stellar metallicities (Fig. 12 and Fig. 13). Such changes then lead to very different predictions for the global Pop III and Pop II star formation rates (Fig. 10), with THESAN able to form Pop III stars down to $z \approx 5$ and the Uniform UVB model curtailing such pathways at $z = 10$. This has clear implications for in-situ and ex-situ star formation contributions to early galaxies, as well as the processing of gas accretion that feeds in-situ star formation (e.g. Kereš et al. 2009; Anglés-Alcázar et al. 2017).

Our results present a troubling picture for the applicability of future and present planned high-resolution simulations to early galaxy formation (e.g. FireBOX; Feldmann et al. 2022). Without the inclusion of a spatially-varying UV background, galaxy properties (in particular the star formation histories of any such galaxies) will be poorly constrained.

We note that any differences seen between THESAN-2 galaxies and those in THESAN-TNG-2 (i.e. with a Uniform UVB) are much smaller when considering lower resolution ($m_{\rm b} \approx 5 \times 10^6$ M$_\odot$), as described in Appendix A of Garaldi et al. (2022). The properties of high-redshift galaxies simulated at lower resolution ($m_{\rm b} \gtrapprox 10^6$ M$_\odot$) are also impacted by the effects discussed in this work; even when including a spatially-varying UV background, they are missing out on an important channel for early galaxy formation (haloes with $M_{\rm H} \approx 10^8$) and their crucial influence of pre-processing and ex-situ star formation even in high mass galaxies. We see good convergence between our models once above the $M_{\rm H} \approx 10^8$ M$_\odot$ threshold, but below this (which is only very marginally resolved in the dark sector, and is poorly resolved in the baryonic sector for the L8N512 volume), significant differences can occur. This is largely due to the artificial suppression of minihalo formation at baryonic mass resolutions $m_{\rm b} \gtrapprox 10^{4.5}$ M$_\odot$, and represents a challenge both from a resolution and physics perspective for ongoing galaxy formation projects. For example, the most realistic simulations of first star and galaxy formation require extended primordial thermochemistry networks including molecular hydrogen formation and self-shielding of LW radiation (see e.g. Greif 2015).

As such, we suggest that authors aiming to study early galaxy formation, which is particularly crucial as we enter the *JWST* era, must use resolutions that allow them to accurately model the formation of minihaloes (i.e. $m_{\rm b} \lessapprox 10^{4.5}$ M$_\odot$ in a typical LCDM cosmology) and must employ a spatially-varying UV background to ensure these haloes can remain self-shielded. We likely would have seen much closer results had we employed a spatially inhomogeneous, semi-numerical, UVB as in e.g. Bird et al. (2022); Trac et al. (2022); Puchwein et al. (2022). Future work should focus on development and self-consistent calibration of such semi-numerical models for existing galaxy formation models, though it remains to be seen whether these semi-numerical treatments can recover the physics seen in fully non-equilibrium simulations. The impact of our small box volume also remains unclear. A larger volume would lead to more variation in galaxy environment, and hence more variation in reionization histories, but would contain higher-mass galaxies that would inevitably lead to more outside-in reionization which is better approximated by the uniform UVB scenario.

Our work also presents observational challenges for lensing fields; if a given region was reionized rapidly, for example a field lying near an overly massive galaxy ($M_* > 10^9$ M$_\odot$), we expect it will have properties similar to our Uniform UVB case, whereas relatively isolated fields should allow minihalo formation to later times. Differences between these two reionization scenarios should be observable within the UVLF, though this is challenging given that we only see differences at $M_{1500} > -12$.

ACKNOWLEDGEMENTS

The authors thank Chris Lovell, Sylvia Ploeckinger, Ewald Puchwein, and John Wise for conversations that contributed to this work. All of the computations were performed on the Engaging cluster supported by the Massachusetts Institute of Technology. MV acknowledges support through NASA ATP 19-ATP19-0019, 19-ATP19-0020, 19-ATP19-0167, and NSF grants AST-1814053, AST-1814259, AST-1909831, AST-2007355 and AST-2107724. AS acknowledges support for Program number *HST*-HF2-51421.001-A provided by NASA through a grant from the Space Telescope Science Institute, which is operated by the Association of Universities for Research in Astronomy, incorporated, under NASA contract NAS5-26555.

Software citations:

- AREPO-RT: Springel (2010); Kannan et al. (2019); Weinberger et al. (2020)
- PYTHON: Van Rossum & Drake Jr (1995)
- MATPLOTLIB: Hunter (2007)
- SCIPY: Virtanen et al. (2020)
- SCIKIT-LEARN: Pedregosa et al. (2011)
- NUMPY: Harris et al. (2020)
- UNYT: Goldbaum et al. (2018)
- SWIFTSIMIO: Borrow & Borrisov (2020); Borrow & Kelly (2021)

- WEBPLOTDIGITIZE: Rohatgi (2022)

DATA AVAILABILITY

All thesan and thesan-hr simulation data will be made publicly available in the near future, including Lyα catalogues. Data will be distributed via `www.thesan-project.com`. Before the public data release, data underlying this article will be shared on reasonable request to the corresponding author(s).

REFERENCES

Anglés-Alcázar D., Faucher-Giguère C.-A., Kereš D., Hopkins P. F., Quataert E., Murray N., 2017, MNRAS, 470, 4698
Atek H., Richard J., Kneib J.-P., Schaerer D., 2018, MNRAS, 479, 5184
Atek H., et al., 2022, arXiv e-prints, p. arXiv:2207.12338
Baek S., Semelin B., Di Matteo P., Revaz Y., Combes F., 2010, A&A, 523, A4
Behroozi P. S., Wechsler R. H., Conroy C., 2013, ApJ, 770, 57
Behroozi P., Wechsler R. H., Hearin A. P., Conroy C., 2019, MNRAS, 488, 3143
Bhatawdekar R., Conselice C. J., Margalef-Bentabol B., Duncan K., 2019, MNRAS, 486, 3805
Bird S., Ni Y., Di Matteo T., Croft R., Feng Y., Chen N., 2022, MNRAS, 512, 3703
Borrow J., Borrisov A., 2020, The Journal of Open Source Software, 5, 2430
Borrow J., Kelly A. J., 2021, arXiv e-prints, p. arXiv:2106.05281
Bouwens R. J., Oesch P. A., Illingworth G. D., Ellis R. S., Stefanon M., 2017, ApJ, 843, 129
Chen P., Wise J. H., Norman M. L., Xu H., O'Shea B. W., 2014, ApJ, 795, 144
Ciardi B., Bolton J. S., Maselli A., Graziani L., 2012, MNRAS, 423, 558
Crain R. A., et al., 2015, MNRAS, 450, 1937
Dubois Y., Devriendt J., Slyz A., Teyssier R., 2012, MNRAS, 420, 2662
Dubroca B., Feugeas J., 1999, Academie des Sciences Paris Comptes Rendus Serie Sciences Mathematiques, 329, 915
Duncan K., et al., 2014, MNRAS, 444, 2960
Efstathiou G., 1992, MNRAS, 256, 43P
Eide M. B., Graziani L., Ciardi B., Feng Y., Kakiichi K., Di Matteo T., 2018, MNRAS, 476, 1174
Eldridge J. J., Stanway E. R., Xiao L., McClelland L. A. S., Taylor G., Ng M., Greis S. M. L., Bray J. C., 2017, Publ. Astron. Soc. Australia, 34, e058
Faucher-Giguère C.-A., Lidz A., Zaldarriaga M., Hernquist L., 2009, ApJ, 703, 1416
Feldmann R., et al., 2022, arXiv e-prints, p. arXiv:2205.15325
Furtak L. J., Shuntov M., Atek H., Zitrin A., Richard J., Lehnert M. D., Chevallard J., 2022, arXiv e-prints, p. arXiv:2208.05473
Garaldi E., Kannan R., Smith A., Springel V., Pakmor R., Vogelsberger M., Hernquist L., 2022, MNRAS, 512, 4909
Gnedin N. Y., 2000, ApJ, 542, 535
Gnedin N. Y., 2014, ApJ, 793, 29
Gnedin N. Y., 2016a, ApJ, 821, 50
Gnedin N. Y., 2016b, ApJ, 825, L17
Gnedin N. Y., Hui L., 1998, MNRAS, 296, 44
Gnedin N. Y., Kaurov A. A., 2014, ApJ, 793, 30
Gnedin N. Y., Madau P., 2022, arXiv e-prints, p. arXiv:2208.02260
Goldbaum N. J., ZuHone J. A., Turk M. J., Kowalik K., Rosen A. L., 2018, The Journal of Open Source Software, 3, 809
Grazian A., et al., 2015, A&A, 575, A96
Graziani L., Salvadori S., Schneider R., Kawata D., de Bennassuti M., Maselli A., 2015, MNRAS, 449, 3137
Greif T. H., 2015, Computational Astrophysics and Cosmology, 2, 3
Guo Y., et al., 2013, ApJS, 207, 24
Haardt F., Madau P., 1996, ApJ, 461, 20
Haardt F., Madau P., 2001, in Neumann D. M., Tran J. T. V., eds, Clusters of Galaxies and the High Redshift Universe Observed in X-rays. p. 64 (`arXiv:astro-ph/0106018`)
Harris C. R., et al., 2020, Nature, 585, 357
Hassan S., Davé R., Finlator K., Santos M. G., 2016, MNRAS, 457, 1550
Hassan S., Davé R., McQuinn M., Somerville R. S., Keating L. C., Anglés-Alcázar D., Villaescusa-Navarro F., Spergel D. N., 2022, ApJ, 931, 62
Hoeft M., Yepes G., Gottlöber S., Springel V., 2006, MNRAS, 371, 401
Hunter J. D., 2007, Computing in Science and Engineering, 9, 90
Iliev I. T., Shapiro P. R., Raga A. C., 2005, MNRAS, 361, 405
Ishigaki M., Kawamata R., Ouchi M., Oguri M., Shimasaku K., Ono Y., 2018, ApJ, 854, 73
Jaacks J., Thompson R., Finkelstein S. L., Bromm V., 2018, MNRAS, 475, 4396
Jaacks J., Finkelstein S. L., Bromm V., 2019, MNRAS, 488, 2202
Kannan R., Vogelsberger M., Marinacci F., McKinnon R., Pakmor R., Springel V., 2019, MNRAS, 485, 117
Kannan R., et al., 2022a, arXiv e-prints, p. arXiv:2210.10066
Kannan R., Garaldi E., Smith A., Pakmor R., Springel V., Vogelsberger M., Hernquist L., 2022b, MNRAS, 511, 4005
Katz H., et al., 2020, MNRAS, 494, 2200
Kawamata R., Ishigaki M., Shimasaku K., Oguri M., Ouchi M., Tanigawa S., 2018, ApJ, 855, 4
Kereš D., Katz N., Davé R., Fardal M., Weinberg D. H., 2009, MNRAS, 396, 2332
Kostyuk I., Nelson D., Ciardi B., Glatzle M., Pillepich A., 2022, arXiv e-prints, p. arXiv:2207.11278
Kulkarni G., Hennawi J. F., Oñorbe J., Rorai A., Springel V., 2015, ApJ, 812, 30
Levermore C. D., 1984, J. Quant. Spectrosc. Radiative Transfer, 31, 149
Livermore R. C., Finkelstein S. L., Lotz J. M., 2017, ApJ, 835, 113
Ma X., et al., 2019, MNRAS, 487, 1844
Marinacci F., et al., 2018, MNRAS, 480, 5113
McKinnon R., Torrey P., Vogelsberger M., 2016, MNRAS, 457, 3775
McKinnon R., Torrey P., Vogelsberger M., Hayward C. C., Marinacci F., 2017, MNRAS, 468, 1505
McLeod D. J., McLure R. J., Dunlop J. S., 2016, MNRAS, 459, 3812
Mesinger A., Furlanetto S., Cen R., 2011, MNRAS, 411, 955
Milosavljević M., Bromm V., 2014, MNRAS, 440, 50
Mitchell P. D., Blaizot J., Cadiou C., Dubois Y., Garel T., Rosdahl J., 2021, MNRAS, 501, 5757
Naiman J. P., et al., 2018, MNRAS, 477, 1206
Nelson D., et al., 2018, MNRAS, 475, 624
Nelson D., et al., 2019a, Computational Astrophysics and Cosmology, 6, 2
Nelson D., et al., 2019b, MNRAS, 490, 3234
O'Shea B. W., Wise J. H., Xu H., Norman M. L., 2015, ApJ, 807, L12
Obreja A., Macciò A. V., Moster B., Udrescu S. M., Buck T., Kannan R., Dutton A. A., Blank M., 2019, MNRAS, 490, 1518
Ocvirk P., et al., 2016, MNRAS, 463, 1462
Ocvirk P., et al., 2020, MNRAS, 496, 4087
Okamoto T., Gao L., Theuns T., 2008, MNRAS, 390, 920
Pakmor R., Springel V., 2013, MNRAS, 432, 176
Pakmor R., Springel V., Bauer A., Mocz P., Munoz D. J., Ohlmann S. T., Schaal K., Zhu C., 2016, MNRAS, 455, 1134
Pallottini A., et al., 2019, MNRAS, 487, 1689
Pallottini A., et al., 2022, MNRAS, 513, 5621
Pawlik A. H., Rahmati A., Schaye J., Jeon M., Dalla Vecchia C., 2017, MNRAS, 466, 960
Pedregosa F., et al., 2011, Journal of Machine Learning Research, 12, 2825
Petkova M., Springel V., 2011, MNRAS, 412, 935
Pillepich A., et al., 2018a, MNRAS, 473, 4077
Pillepich A., et al., 2018b, MNRAS, 475, 648
Pillepich A., et al., 2019, MNRAS, 490, 3196
Planck Collaboration et al., 2016, A&A, 594, A13
Planck Collaboration et al., 2020, A&A, 641, A10
Ploeckinger S., Schaye J., 2020, MNRAS, 497, 4857
Puchwein E., et al., 2022, arXiv e-prints, p. arXiv:2207.13098
Rahmati A., Schaye J., 2014, MNRAS, 438, 529

Rees M. J., 1986, MNRAS, 218, 25P
Rohatgi A., 2022, Webplotdigitizer: Version 4.6, https://automeris.io/WebPlotDigitizer
Rorai A., et al., 2017, Science, 356, 418
Rosdahl J., et al., 2018, MNRAS, 479, 994
Rosdahl J., et al., 2022, MNRAS, 515, 2386
Ross H. E., Dixon K. L., Iliev I. T., Mellema G., 2017, MNRAS, 468, 3785
Santos M. G., Ferramacho L., Silva M. B., Amblard A., Cooray A., 2010, MNRAS, 406, 2421
Sarmento R., Scannapieco E., 2022, ApJ, 935, 174
Schauer A. T. P., Boylan-Kolchin M., Colston K., Sameie O., Bromm V., Bullock J. S., Wetzel A., 2022, arXiv e-prints, p. arXiv:2210.12815
Schaye J., Theuns T., Rauch M., Efstathiou G., Sargent W. L. W., 2000, MNRAS, 318, 817
Schaye J., et al., 2015, MNRAS, 446, 521
Semelin B., Eames E., Bolgar F., Caillat M., 2017, MNRAS, 472, 4508
Shapiro P. R., Giroux M. L., Babul A., 1994, ApJ, 427, 25
Shapiro P. R., Iliev I. T., Raga A. C., 2004, MNRAS, 348, 753
Shen X., et al., 2020, MNRAS, 495, 4747
Shen X., Vogelsberger M., Nelson D., Tacchella S., Hernquist L., Springel V., Marinacci F., Torrey P., 2022, MNRAS, 510, 5560
Smith B. D., Wise J. H., O'Shea B. W., Norman M. L., Khochfar S., 2015, MNRAS, 452, 2822
Smith A., Kannan R., Garaldi E., Vogelsberger M., Pakmor R., Springel V., Hernquist L., 2022, MNRAS, 512, 3243
So G. C., Norman M. L., Reynolds D. R., Wise J. H., 2014, ApJ, 789, 149
Song M., et al., 2016, ApJ, 825, 5
Springel V., 2005, MNRAS, 364, 1105
Springel V., 2010, MNRAS, 401, 791
Springel V., 2011, in Computational Star Formation. pp 203–206, doi:10.1017/S1743921311000378
Springel V., Hernquist L., 2003, MNRAS, 339, 289
Springel V., et al., 2018, MNRAS, 475, 676
Springel V., Pakmor R., Zier O., Reinecke M., 2021, MNRAS, 506, 2871
Tacchella S., Bose S., Conroy C., Eisenstein D. J., Johnson B. D., 2018, ApJ, 868, 92
Tacchella S., et al., 2022, ApJ, 927, 170
Theuns T., Schaye J., Haehnelt M. G., 2000, MNRAS, 315, 600
Trac H., Chen N., Holst I., Alvarez M. A., Cen R., 2022, ApJ, 927, 186
Trebitsch M., Blaizot J., Rosdahl J., Devriendt J., Slyz A., 2017, MNRAS, 470, 224
Van Rossum G., Drake Jr F. L., 1995, Python reference manual. Centrum voor Wiskunde en Informatica Amsterdam
Virtanen P., et al., 2020, Nature Methods, 17, 261
Vogelsberger M., Sijacki D., Kereš D., Springel V., Hernquist L., 2012, MNRAS, 425, 3024
Vogelsberger M., Genel S., Sijacki D., Torrey P., Springel V., Hernquist L., 2013, MNRAS, 436, 3031
Vogelsberger M., et al., 2014, MNRAS, 444, 1518
Vogelsberger M., et al., 2020, MNRAS, 492, 5167
Weinberger R., et al., 2017, MNRAS, 465, 3291
Weinberger R., Springel V., Pakmor R., 2020, ApJS, 248, 32
Whitler L. R., Mason C. A., Ren K., Dijkstra M., Mesinger A., Pentericci L., Trenti M., Treu T., 2020, MNRAS, 495, 3602
Wilkins S. M., et al., 2022, MNRAS,
Wise J. H., 2019, arXiv e-prints, p. arXiv:1907.06653
Wise J. H., Abel T., 2008, ApJ, 685, 40
Wise J. H., Abel T., Turk M. J., Norman M. L., Smith B. D., 2012a, MNRAS, 427, 311
Wise J. H., Turk M. J., Norman M. L., Abel T., 2012b, ApJ, 745, 50
Wise J. H., Demchenko V. G., Halicek M. T., Norman M. L., Turk M. J., Abel T., Smith B. D., 2014, MNRAS, 442, 2560
Wu X., Kannan R., Marinacci F., Vogelsberger M., Hernquist L., 2019, MNRAS, 488, 419
Xu H., Norman M. L., O'Shea B. W., Wise J. H., 2016, ApJ, 823, 140
Yeh J. Y. C., et al., 2022, arXiv e-prints, p. arXiv:2205.02238
Zhu H., Avestruz C., Gnedin N. Y., 2020, ApJ, 899, 137

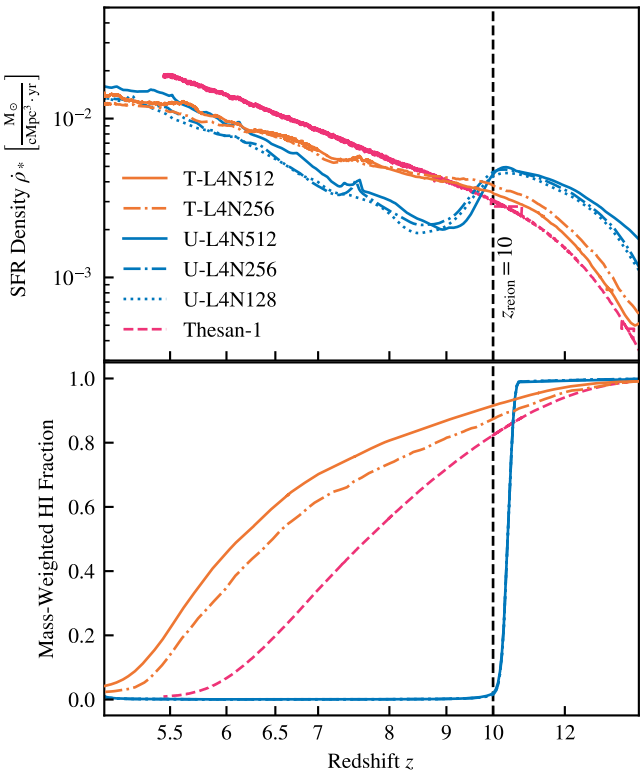


Figure A1. Analogue of Fig. 2, which shows the star formation rate density of the volumes with the THESAN model and the Uniform UVB model (line colours). The different line styles show different simulation resolutions, from the highest resolution used here to one comparable to the original THESAN-1 simulation.

APPENDIX A: RESOLUTION CONVERGENCE

In Fig. A1, we demonstrate the convergence properties of our simulations. Here, we show simulations of the same L4 volume at various resolutions: L4N512 (as in the main text), L4N256, at the same mass resolution as the L8N512 volume, and L4N128, which is at a resolution 8 times lower (comparable to Thesan-1). We see that the star formation rate density is mainly dependent on the choice of reionization model, *not* on the resolution that the volume is simulated at. This indicates the differences between the star formation histories of L8N512 and L4N512 in Fig. 2 are mainly driven by the different phases and volumes than they are by differences between baryonic resolution.

In Fig. A2 we show the optical depth to the CMB as a function of redshift for our models at various resolutions. We see, as expected, that the THESAN-HR volumes (orange lines) under-shoot the Planck Collaboration et al. (2020) results due to their systematically late reionization, originating from the lack of bright sources in these small volumes. We see a small difference between resolution levels that is entirely consistent with the differences seen in the star formation history (see Fig. A1) and associated small change in the ionising photon budget. As shown in Kannan et al. (2022b) the THESAN-1 volume matches the available Planck data well. Finally, the models employing a uniform UVB lead to systematically high optical depths due to their vastly different (and earlier) reionization histories.

This paper has been typeset from a TEX/LATEX file prepared by the author.

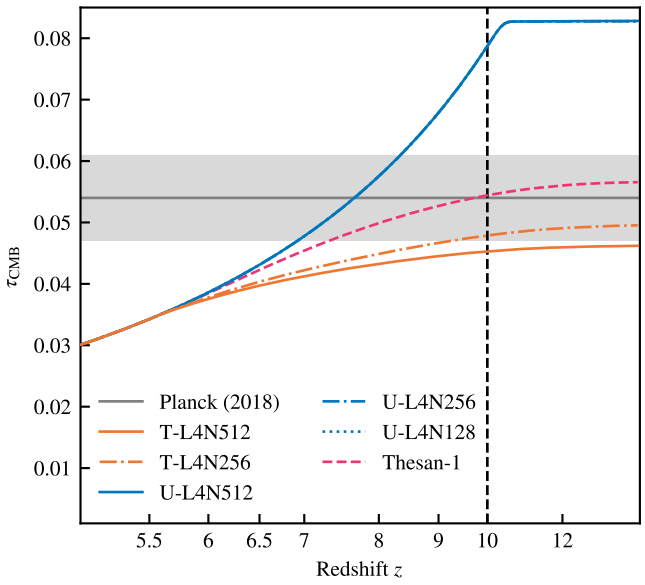


Figure A2. The optical depth to the CMB as a function of redshift, for the convergence volumes with a uniform UVB (blue lines) and with the standard THESAN full radiative transfer treatment (orange lines). We show, for comparison, the original THESAN-1 simulation (pink) and the results from Planck Collaboration et al. (2020).